Modeling ultrasonic vibration fatigue with unified mechanics theory

Article *in* International Journal of Solids and Structures · October 2021

DOI: 10.1016/j.ijsolstr.2021.111313

Hsiaowei Lee
University at Buffalo, The State University of New York

Cemal Basaran
University at Buffalo, The State University of New York

Halina Egner
Cracow University of Technology

Adam Lipski
Bydgoszcz University of Science and Technology, Faculty of Mechanical Engineeri…

International Journal of Solids and Structures 236–237 (2022) 111313

Contents lists available at ScienceDirect

International Journal of Solids and Structures

journal homepage: www.elsevier.com/locate/ijsolstr

Modeling ultrasonic vibration fatigue with unified mechanics theory

Hsiao Wei Lee [a], Cemal Basaran [a,*], Halina Egner [b], Adam Lipski [c], Michał Piotrowski [c], Stanisław Mroziński [c], Noushad Bin Jamal M [d], Chebolu Lakshmana Rao [d]

[a] *Civil, Structural and Environmental Engineering, University at Buffalo, New York, United States*
[b] *Institute of Applied Mechanics, Faculty of Mechanical Engineering, Cracow University of Technology, PL 31-864 Kraków, Al. Jana Pawła II 37, Poland*
[c] *Faculty of Mechanical Engineering, UTP University of Science and Technology, PL 85-796 Bydgoszcz, Al. prof. S. Kaliskiego 7, Poland*
[d] *Department of Applied Mechanics, Indian Institute of Technology, Madras, India*

ARTICLE INFO

Keywords:
Entropy
Unified mechanics theory
Thermodynamics
Metal fatigue
Ultrasonic vibration testing
Dynamics

ABSTRACT

A series of ultrasonic vibration tests are performed on A656 grade steel samples, at a frequency of 20 kHz. A fatigue life model based on the unified mechanics theory is introduced to predict the very high cycle fatigue life of metals. Then, the fatigue life test data results are compared with the unified mechanics theory based model simulation results. It is shown that the physics-based unified mechanics theory can predict very high cycle fatigue life very well, without the need for the traditional empirical curve fitting a fatigue damage evolution function. The model does not require any curve fitting parameters obtained from fatigue test data. However, it does require deriving analytical thermodynamic fundamental equation of the material subjected to ultrasonic vibration fatigue. The thermodynamic fundamental equation of the material formulates the entropy generation mechanisms during the fatigue process. There are more than half a dozen entropy generation mechanisms during fatigue process. Entropy is an additive property, hence, the entropy generation due to all active mechanisms can be added.

1. Introduction

Fatigue life models primarily rely on test data for curve fitting a degradation evolution function, because the Newtonian x, y, z, space–time coordinate system does not include an axis for dissipation, degradation mechanism, or irreversible processes. As a result, stress, strain, or dissipated energy have been used as a variable of an empirical function to establish fatigue life prediction models. An extensive literature survey of fatigue life prediction models is recently published (Lee and Basaran, 2021), hence it is not necessary to repeat a literature survey herein.

In unified mechanics theory (UMT) degradation occurs along the Thermodynamic State Index (TSI) axis, [a fifth linearly independent axis àla Boltzmann 1877], according to the fundamental equation of the material and Boltzmann entropy formulation (Basaran, 2021).

The laws of unified mechanics theory are given as follows (Basaran, 2021).

Second Law: Initial momentum of a body will degrade according to the second law of thermodynamics, (Basaran, 2021)

$$(1-\phi)Fdt = d(mv) \tag{1}$$

where $(1-\phi)F$ is the force as a function of the thermodynamic state index which governs the dissipation in momentum.

Third Law: Initial reaction of a body in response to an action will change over time as the stiffness degrades according to the second law of thermodynamics and its thermodynamic fundamental equation, (Basaran, 2021)

$$F_{12} = F_{21} = \frac{d\left[\frac{1}{2}K_{21}(1-\phi){u_{21}}^2\right]}{du_{21}} \tag{2}$$

where F_{12} is the acting force, F_{21},and u_{21} are the reaction, and displacement in the reacting system, $[K_{21}(1-\phi)]$ is the reacting stiffness which is a function of the thermodynamic state index which governs the degradation of the reacting system according to the thermodynamic fundamental equation of the material. Eqs. ((1) and (2)) denote that, a physical system subjected to a change in the space–time coordinate system also undergoes dissipation processes, which changes its coordinate on the thermodynamic state index axis. The Newton's universal laws of motion define the space–time coordinates of a material point in a physical system subjected to a loading. The laws of thermodynamics, on

---

* Corresponding author.
E-mail address: cjb@buffalo.edu (C. Basaran).

https://doi.org/10.1016/j.ijsolstr.2021.111313
Received 9 June 2021; Received in revised form 11 September 2021; Accepted 18 October 2021
Available online 27 October 2021
0020-7683/Published by Elsevier Ltd.

Nomenclature

ϕ	Thermodynamic state indexther
ϕ_{cr}	Critical thermodynamic state index
Δs	Change of total specific entropy
m_s	Molar mass of the material
R	Universal gas constant
S_T	thermal conduction entropy
S_r	Internal friction entropy
$S_{\mu p}$	Microplasticity entropy
k_h	Thermal conductivity
$\boldsymbol{\sigma}^{\mu}$	Microscopic stress tensor
$\boldsymbol{\varepsilon}_e^{\mu}$	Microscopic elastic strain tensor
$\boldsymbol{\varepsilon}_p^{\mu}$	Microscopic plastic strain tensor
$\boldsymbol{\Sigma}$	Macroscopic stress tensor
$\boldsymbol{E}$	Macroscopic strain tensor
f_v	Volume fraction of activated micro-defects
$\boldsymbol{S}^{\mu}$	Microscopic deviatoric stress
$\boldsymbol{\alpha}^{\mu d}$	Deviatoric of microscopic back stress
$\boldsymbol{e}^{\mu p}$	Microscopic equivalent plastic strain
h	Hardening modulus
σ_y	Microscopic yield stress (fatigue limit)
Ψ_f	Frequency coefficient
ρ	Mass density
r	Internal friction [IF] generated heat
r^{drag}	IF due to drag mechanism
r^{dis}	IF due to dislocation motion
B^{drag}	Drag coefficient
v	Dislocation velocity
μ	Shear modulus
b	Magnitude of Burgers vector
ϱ	Total dislocation density
ϱ_m	Mobile dislocation density
α_H	Taylor's constant
$\dot{\gamma}$	Shear strain rate
a	Lattice constant
E	Young's modulus
υ	Poisson's ratio
α	Thermal expansion coefficient
c_V	Specific heat capacity
θ	Total change in temperature
τ_{eq}	Conduction time constant
ℓ_{eq}	Fraction of heat conducted

the other hand, define the coordinate of a physical system on the thermodynamic state index axis.

Thermodynamic State Index (TSI), ϕ, is given by, (Basaran, 2021)

$$\phi = \phi_{cr}\left[1-\exp\left(\frac{-\Delta s \bullet m_s}{R}\right)\right] \tag{3}$$

in which

$$\phi_{cr} = \frac{\phi}{Factor\ of\ safety} \tag{4}$$

In Eqs. ((3) and (4)), ϕ_{cr} is the user-defined critical value of TSI, Δs is total specific entropy change of the system with respect to a reference state, m_s is the molar mass and R is the gas constant. The calculation of ϕ requires deriving the thermodynamic fundamental equation analytically. Details of the unified mechanics theory are given extensively in (Basaran, 2021). Hence, mathematical details of the theory are not repeated in here.

Any microstructural state of the material can be defined as a reference state for a closed, adiabatic system. It can be assumed that the TSI is $\phi = 0$ at the "initial" reference state. However, ϕ does not have to be taken as zero initially. After fatigue failure material reaches a critical thermodynamic state, entropy in the system reaches a maximum, and the entropy generation rate becomes zero.

Unified mechanics theory, (Basaran, 2021), unifies the universal laws of motion of Newton and the second law of thermodynamics at the ab-initio level. As a result, governing differential equation of any system automatically includes entropy generation. The relation between entropy generation and degradation of materials is well established in the literature, (Lee and Basaran, 2021; Basaran, 2021; Kondepudi and Prigogine, 2014; Boltzmann, 1877; Planck, 1900; Basaran and Yan, 1998; Bryant et al., 2008; Lemaitre and Chaboche, 1990; Basaran and Chandaroy, 2000; Basaran et al., 2003; Basaran and Nie, 2004; Basaran et al., 2004; Ye et al., 2004; Ye et al., 2006; Basaran and Lin, 2007; Basaran and Lin, 2007; Basaran et al., 2008; Li et al., 2008; Basaran and Lin, 2008; Li et al., 2009; Basaran et al., 2009; Yao and Basaran, 2012; Yao and Basaran, 2013; Yao and Basaran, 2013; Yao and Basaran, 2013; Temfack and Basaran, 2015; Bin Jamal et al., 2019; Lee and Basaran, 2021; Mehdizadeh et al., 2021; Hajshirmohammadi and Khonsari, 2020; Wang and Yao, 2019; Young and Subbarayan., 2019; Osara and Bryant., 2019; Egner et al., 2020; Ribeiro et al., 2020; Teng et al., 2020; Naderi et al., 2009; Wang and Yao, 2017; Yun and Modarres, 2019; Zhao et al., 2000; Basaran et al., 2001). The thermodynamic state index axis of the unified mechanics theory maps the entropy generation rate between zero and one, according to the thermodynamic fundamental equation of the material. The thermodynamic lifespan of any closed system travels between 0 and 1 along this axis. (Basaran, 2021)

Fig. 1-1 shows the coordinate system in unified mechanics theory. It is important to emphasize that in the UMT coordinate system derivative of displacement with respect to entropy is not zero because TSI is a linearly independent axis.

In the unified mechanics theory, there are 5 linearly independent axes. In addition to Newtonian space–time axes, there is Thermodynamic State Index (TSI) axis. As a result, the derivatives with respect to entropy are not zero, as in Newtonian mechanics. This can be explained by the following example; physical state of a 50-year-old person with terminal illness and a 100-year-old sick person cannot be defined in Newtonian space–time coordinates. As a result, they have different coordinates on the time axis, 50 years and 100 years, respectively. On the other hand, in unified mechanics theory their physical thermodynamic state is represented by the TSI axis coordinate in addition to the space–time coordinates. On TSI axis these two individuals, 50-year-old person with terminal illness and a sick 100-year-old man will have the same thermodynamic state index axis coordinate, $\Phi = 0.999$,. They have about the same remaining life on TSI axis. Essentially, a person's age on time axis, does not give any information about that person's thermodynamic physical state.

The concept of using entropy as a damage metric to predict fatigue life has been used extensively for thermal, mechanical, chemical and electrical loadings, but never for ultrasonic vibration fatigue life predictions, (Lee and Basaran, 2021; Basaran, 2021; Basaran and Yan, 1998; Bryant et al., 2008; Lemaitre and Chaboche, 1990; Basaran and Chandaroy, 2000; Basaran et al., 2003; Basaran and Nie, 2004; Basaran et al., 2004; Ye et al., 2004; Ye et al., 2006; Basaran and Lin, 2007; Basaran and Lin, 2007; Basaran et al., 2008; Li et al., 2008; Basaran and Lin, 2008; Li et al., 2009; Basaran et al., 2009; Yao and Basaran, 2012; Yao and Basaran, 2013; Yao and Basaran, 2013; Yao and Basaran, 2013; Temfack and Basaran, 2015; Bin Jamal et al., 2019; Lee and Basaran, 2021; Mehdizadeh et al., 2021; Hajshirmohammadi and Khonsari, 2020; Wang and Yao, 2019; Young and Subbarayan., 2019; Osara and Bryant.,

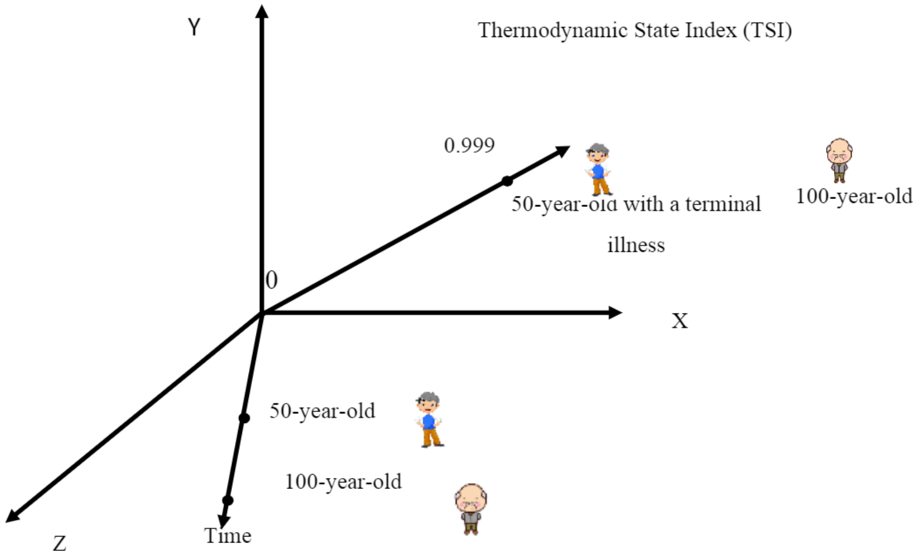

Fig. 1-1. Coordinate system in unified mechanics theory.

2019; Egner et al., 2020; Ribeiro et al., 2020; Teng et al., 2020; Naderi et al., 2009; Wang and Yao, 2017; Yun and Modarres, 2019). Details of the formulation and experimental verification of the unified mechanics theory are available in the literature.

In this study, the objective is to develop a fatigue life model for metals subjected to ultrasonic vibration with maximum nominal stress below the yield stress of the material. In Section 2, the thermodynamic fundamental equation [entropy generation equation] used to calculate thermodynamic state index ϕ is introduced. In Section 3, the experimental setup and test results for ultrasonic fatigue of EN 1.0577 steel are presented. In Section 4, the amount of entropy generation from each mechanism is presented. Then, TSI evolution is used to predict the ultrasonic fatigue life of the specimen, and simulation results are compared with the test data.

2. Derivation of thermodynamic fundamental equation for ultrasonic fatigue: Entropy generation mechanisms

For the very high cycle fatigue of metals, there are six prominent mechanisms that generate entropy (Lee and Basaran, 2021). These are: configurational entropy due to the permutation of atomic vacancies, S_c, vibrational entropy, S_{vib}(Kelly and Knowles, 2012; Abbaschian et al., 2010; Fultz, 2010), the entropy generation due to vacancy concentration gradient driven diffusion S_d (Basaran and Lin, 2007; Yao and Basaran, 2012; Ye et al., 2004; Ye et al., 2006; Basaran and Lin, 2008; Li et al., 2009), the entropy generation due to heat conduction S_T(Basaran and Lin, 2007; Lee and Basaran, 2021; Basaran, 2021; Basaran et al., 2008; Li et al., 2008; Yao and Basaran, 2013; Yao and Basaran, 2013; Yao and Basaran, 2013), the entropy generation due to internal atomic-friction-generated heat S_r(Basaran, 2021; Basaran and Nie, 2004), and finally the entropy generation due to micro-plasticity, $S_{\mu p}$ (Lemaitre et al., 1999; Doudard et al., 2005; Charkaluk and Constantinescu, 2009; Fan et al., 2018). Among these six mechanisms, the first three are too small compared to other mechanisms (Lee and Basaran, 2021). Therefore, in this section, we only discuss the entropy generation due to the last three mechanisms. Entropy is an additive property; hence, we can write the following equation for the total entropy change to obtain the thermodynamic fundamental equation,

$$\Delta S = \Delta S_T + \Delta S_r + \Delta S_{\mu p} \tag{5}$$

The following assumptions are made in the study:

1. Maximum nominal stress is below the yield stress of the material hence no macroscopic plastic deformation is observed. However, a mechanism called micro-plasticity is expected to happen at defect sites at the micro-level, (Lemaitre et al., 1999; Doudard et al., 2005; Charkaluk and Constantinescu, 2009; Fan et al., 2018).
2. Input mechanical energy increases atomic vacancies and dislocation densities. However, the increasing dislocation density only causes hardening at a micro-level and never induces macroscopic plastic deformation, as the maximum nominal stress is below the metal yield stress. The vacancy generation/diffusion and dislocation motions (e.g., cross-slip) around inclusions induce plasticity at a micro-level, (Callister and Rethwisch, 2018; Marti et al., 2020; Mughrabi, 2013; Ho et al., 2017; Mughrabi, 2009).
3. Temperature evolution in the specimen is due to internal atomic-friction-generated heat, heat conduction, microplastic work and thermo-elastic damping.

2.1. Entropy generation due to heat conduction

Temperature gradient causes an irreversible heat flow across the specimen during fatigue loading, as shown in section 3 Fig. 3-2.a-d. The entropy change equation is given by (Basaran, 2021; Basaran and Lin, 2007; Basaran et al., 2008; Li et al., 2008; Yao and Basaran, 2013; Yao and Basaran, 2013; Yao and Basaran, 2013)

$$\Delta S_T = -\int_{t_0}^{t}\left(k_h\frac{\nabla T\bullet\nabla T}{T^2}\right)dt \tag{6}$$

where k_h is coefficient of heat conduction, ∇T is the temperature gradient from the gage section to the grip section, t_0 and t are the point in time when specimen is initially sitting at room temperature and rising in temperature due to self-heating, respectively. T in the denominator is the absolute temperature on the surface of the specimen focusing on the gage center, which will be evaluated later in section 4.3.

In Eq. (6), the amount of entropy change due to heat conduction is strongly dependent on the test duration. To calculate the order of magnitude of this entropy generation mechanism for ultrasonic vibration fatigue, the following boundary conditions [from Section 3.7] are used:

The temperature at the gage section of an EN 1.0577 steel test specimen raises from room temperature (300 K) to around 450 K at failure under ultrasonic vibration fatigue test with 400 MPa stress amplitude. Thermal conductivity of $k_h = 50\mathrm{WK}^{-1}\mathrm{m}^{-1}$ is used. We assume the temperature varies parabolically along the centerline of the sample from the gage section to the grip section, as $T = C_1x^2 + C_2x + C_3$. If the boundary condition is set to be $T_{gage}(t) = T(x = 0,t)$, $T_{grip}(t) = T(x = \pm L/2, t)$ where $L/2 = 30mm$ is the length between gage and grip sections, a simple one-dimensional thermal gradient that changes as the number of cycles increases can be obtained $\nabla T = \frac{8x}{L^2}(T_{grip}(t) - T_{gage}(t))$. Using Eq. (6), the entropy change due thermal-conduction calculated is shown in section 4, Fig. 4-2.

2.2. Entropy generation due to micro-plasticity

During very high cycle fatigue, microplasticity happens at defect sites. A microplasticity model developed by Lemaitre (Lemaitre et al., 1999) and then reformulated by Doudard (Doudard et al., 2005) is used to calculate the entropy generation due to this process. The term “micro-plasticity” is normally used in two scale models. The material is investigated at macroscopic and microscopic scales, independently. At the macroscopic scale, the material deforms elastically while at the microscopic scale micro-plasticity occurs, because of high stress concentrations at defects and at localized dislocation slip planes (Lemaitre et al., 1999; Doudard et al., 2005; Charkaluk and Constantinescu, 2009; Fan et al., 2018).

The two-scale model is based on an RVE (Representative Volume Element) and divides a continuum into two parts: elastic matrix and elastic–plastic inclusions. The law of localization and homogenization is utilized to establish a relationship between macroscopic stress tensor and the microscopic stress and microscopic plastic strain tensors (Charkaluk and Constantinescu, 2009; Fan et al., 2018). Charkaluk and Constantinescu (Charkaluk and Constantinescu, 2009) derived a macro to micro relation of the stress and strain using Kroner’s self-consistent scheme (Kröner, 1961), as follows,

$$\boldsymbol{\sigma}^{\mu} = \boldsymbol{\Sigma} - 2\mu(1-b)(1-f_v)\boldsymbol{\varepsilon}_P^{\mu} \tag{7}$$

$$\boldsymbol{\varepsilon}_e^{\mu} = \boldsymbol{E} - [(1-b)(1-f_v)]\boldsymbol{\varepsilon}_P^{\mu} \tag{8}$$

where μ is the Lamé constant, b is a material parameter [function of Lamé constant and bulk modulus], and f_v is the volume fraction of activated micro-defects experiencing microplasticity

$$f_v = \frac{V_D}{V_{matrix}} \tag{9}$$

where V_D is the activated volume of the micro-defects, V_{matrix} is the volume of the elastic matrix. The relative surface ratio covered by activated micro slip bands at the center of samples’ gauge part represent the variable f_v in references (Charkaluk and Constantinescu, 2009; Cugy and Galtier, 2002). In this study, we used the fractography results (SEM images) of the failed specimen’s, as shown in Fig. 3.13, to estimate f_v value using a technique used in literature (Charkaluk and Constantinescu, 2009). The f_v is determined to be 20%.Fig. 2.1

The microplasticity model proposed by Charkaluk and Constantinescu (Charkaluk and Constantinescu, 2009) is given by,

$$\Delta\boldsymbol{\varepsilon}_P^{\mu} = \frac{\sqrt{\frac{3}{2}}\|\boldsymbol{A}_{n+1}^{*}\| - \sigma_y}{\sqrt{\frac{3}{2}}\left(2\mu(1-b)(1-f_v) + \frac{2}{3}h\right)}\frac{\boldsymbol{A}_{n+1}^{*}}{\|\boldsymbol{A}_{n+1}^{*}\|} \tag{10}$$

in which h is the hardening modulus, and

$$\boldsymbol{A}_{n+1}^{*} = \mathrm{dev}(\boldsymbol{\Sigma}_n) - \left(2\mu(1-b)(1-f_v) + \frac{2}{3}h\right)\boldsymbol{\varepsilon}_{p,n}^{\mu} + \mathrm{dev}(\boldsymbol{\Delta\Sigma})$$

$$b = \frac{6(K+2\mu)}{5(3K+4\mu)} \tag{11}$$

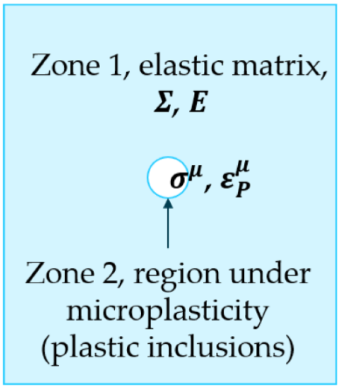

Fig. 2-1. A representative volume element of the two-scale model, $\boldsymbol{\Sigma}$ is macroscopic elastic stress tensor, $\boldsymbol{E}$ is macroscopic elastic strain tensor, $\boldsymbol{\sigma}^{\mu}$ is microscopic stress tensor, $\boldsymbol{\varepsilon}_P^{\mu}$ is microscopic plastic strain tensor.

where $\boldsymbol{A}_{n+1}^{*}$ is the trial step for the deviatoric part of the relative stress tensor $\boldsymbol{\sigma}^{\mu^*}$ defined as $\boldsymbol{A} = \mathrm{dev}(\boldsymbol{\sigma}^{\mu^*})$, $\boldsymbol{\sigma}^{\mu^*} = \boldsymbol{\sigma}^{\mu} - \frac{2}{3}h\boldsymbol{\varepsilon}_P^{\mu}$. For the micro-plasticity model, we utilize linear kinematic hardening. The yield criterion is given by (Ohno, 2001);

$$f = \left(\boldsymbol{S}^{\mu} - \boldsymbol{\alpha}^{\mu d}\right) : \left(\boldsymbol{S}^{\mu} - \boldsymbol{\alpha}^{\mu d}\right) - \frac{2}{3}\left(\sigma_{y0}^{\mu}\right)^2 = 0 \tag{12}$$

and the kinematic hardening rule is given by

$$\dot{\boldsymbol{\alpha}}^{\mu} = h\dot{\boldsymbol{e}}^{\mu p}\frac{1}{\sigma_{y0}^{\mu}}(\boldsymbol{\sigma}^{\mu} - \boldsymbol{\alpha}^{\mu}) = h\sqrt{\frac{2}{3}\dot{\varepsilon}_{ij}^{\mu p}\dot{\varepsilon}_{ij}^{\mu p}}\ \frac{1}{\sigma_{y0}^{\mu}}(\boldsymbol{\sigma}^{\mu} - \boldsymbol{\alpha}^{\mu}) \tag{13}$$

where $\boldsymbol{S}^{\mu}$ is the microscopic deviatoric stress, $\boldsymbol{\alpha}^{\mu d}$ is the deviatoric part of the microscopic back stress, $\boldsymbol{e}^{\mu p}$ is the microscopic equivalent plastic strain, σ_{y0}^{μ} is the microscopic yield stress,$(\boldsymbol{\sigma}^{\mu} - \boldsymbol{\alpha}^{\mu})$ is the translational direction of the microscopic yield surface under Ziegler’s rule, h is the kinematic linear hardening modulus defined as the slope of the stress–strain curve for a finite plastic strain value,$h = (\sigma^{\mu} - \sigma_{y0}^{\mu})/\varepsilon^{\mu p}$.

The entropy change equation due to microplasticity can be given by (Basaran, 2021; Basaran and Yan, 1998; Basaran and Nie, 2004; Basaran et al., 2004; Bin Jamal et al., 2019; Lee and Basaran, 2021)

$$\Delta S_{\mu p} = \int_{t_0}^{t}\Psi_f\left(\phi f_v\frac{\boldsymbol{\sigma}^{\mu} : \dot{\boldsymbol{\varepsilon}}_P^{\mu}}{T}\right)dt \tag{14}$$

In which Ψ_f is a frequency coefficient, ϕ is the thermodynamic state index, f_v is defined as the maximum percentage of dislocation planes that can be activated, which can be determined by using the percentage of the observed active slip bands’ area in the center of specimen’s gauge part, as illustrated in Fig. 2-2. T in the denominator is the absolute temperature on of the specimen which will be evaluated later in Section 4.3. During the microscopic plastic slip, some plastic work is stored as dislocation stored energy. This stored dislocation energy is accounted for in the hardening of the material, which is included in Eq. (13).

Fig. 2-2 shows the Illustration of microplasticity. Inside the hexagon region, microscopic stress and microplastic strain at each microplasticity inclusion are computed under the laws of localization and homogenization.

The frequency coefficient Ψ_f is to relate the loading machine operating frequency with entropy generation rate. It is well understood that the fatigue life measured for a specimen is affected by the loading frequency. For example, under the same stress amplitude, fatigue life is shorter when loading is at 10 Hz to 50 Hz frequency range, than the fatigue life when loading frequency range is 15 kHz to 30 kHz. For FCC metals, it is well known that the difference in fatigue life is due to the occurrence of time-dependent cross slip of dislocations and vacancy production/diffusion involved in the persistent slip band formation

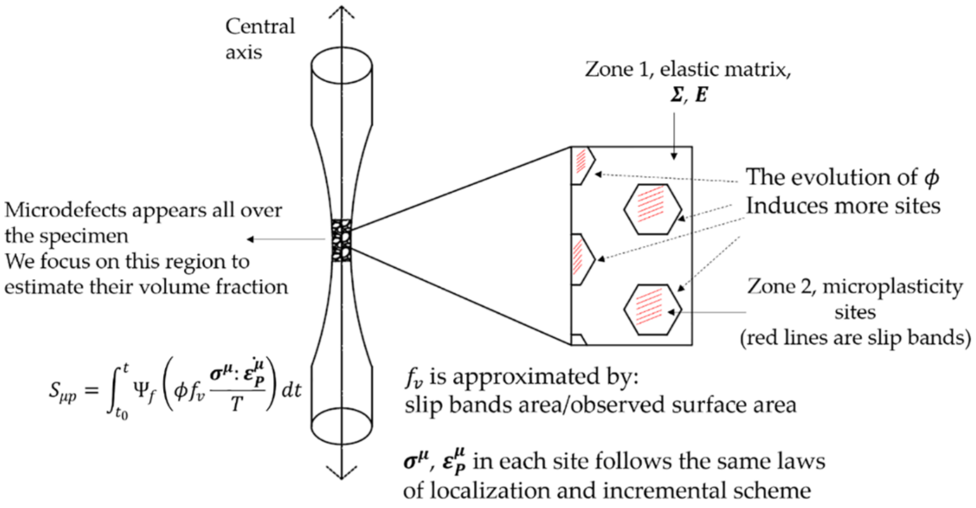

Fig. 2-2. Illustration of microplasticity entropy calculation.

(Marti et al., 2020).

Marti et al (Marti et al., 2020) established a correlation between low and high frequency fatigue life of pure polycrystalline copper with mechanisms of slip band formation. The failure and early slip marking S–N curves they obtained from experiments show that the fatigue life is longer at higher frequencies, and the number of cycles for early slip markings to emerge is also higher at "high" than "low" frequencies, for a given stress amplitude (Zhao et al., 2000; Basaran et al., 2001). The similarity of these tendencies suggests a correlation between both failure and early slip marking S-N curves. They assume such correlation is a reasonable hypothesis because the formation and emergence of slip bands play a key role in crack initiation and fatigue failure in ductile single-phase metals. Similar results have been reported in (Zhao et al., 2000; Basaran et al., 2001). The initiation of persistent slip bands at the surface of fatigued specimens requires cross slip of screw dislocations to promote slip localization and irreversibility. In addition, the generation of vacancies in persistent slip bands and their diffusion towards the matrix favor their emergence. They concluded that the cross-slip activation is the main mechanism that leads to early slip markings.

For the ultrasonic vibration of BCC metals, Torabian et al (Torabian et al., 2017) reported that there is a transition between material deformation mode from thermally-activated regime at stress amplitudes below the fatigue limit to athermal mode at stress amplitudes above the fatigue limit. In this paper, since we are applying a macroscopic stress amplitude above the fatigue limit [while below the macroscopic yield stress], the athermal regime where the mobilities of screw and edge dislocations are equivalent and screw dislocations can cross slip, is of our interest.

The cross-slip probability P is given by (Marti et al., 2020);

$$P = \beta \frac{l}{l_0} \frac{\delta t}{t_0} \exp\left(\frac{\tau_{css} - \tau_{csR}}{k_B T} V\right) \tag{15}$$

where β is a normalization coefficient ensuring that $0 < P < 1$, l/l_0 is the ratio of the length of a screw dislocation segment to a reference length $l_0 = 1$ mm, $\delta t/t_0$ is the ratio of the considered time to a reference time, V is the activation volume associated with cross slip, $(\tau_{css} - \tau_{csR})$ compares the resolved shear stress τ_{css} on the cross slip system to a threshold critical stress τ_{csR} required to activate cross slip, k_B is the Boltzmann's constant, and T is the absolute temperature.

The duration during which τ_{css} is greater than τ_{csR} in 1 cycle can be given by (Marti et al., 2020)

$$\Delta t_{1cycle} = \left(1 - \frac{2\arcsin\left(\frac{\tau_{csR}}{\tau_{css}}\right)}{\pi} \right) \frac{1}{f} \tag{16}$$

where f is the frequency of cyclic loading. Assuming all the parameters in equation (15) are frequency insensitive, equation (16) shows that the time duration to activate cross slip is inversely related to the frequency. For two different loading frequencies, 30 Hz and 20 kHz at the same given stress amplitude, the following equation must be satisfied in order to obtain the same cumulated probability of cross slip activation,

$$T_A = \Delta t_{1cycle,30Hz} \times N_{30Hz} = \Delta t_{1cycle,20kHz} \times N_{20kHz} \tag{17}$$

where T_A is the duration when τ_{css} is greater than τ_{csR}, N is the number of cycles.

According to Eqs. (16) and (17), at a given stress amplitude the material subjected to f_1 loading frequency reaches the same cumulative probability of activating initial micro-defects (early slip marking) as the material under f_2 loading frequency when,

$$\frac{N_1}{N_2} = \frac{f_1}{f_2} \tag{18}$$

where N_1 is the number of cycles performed under f_1 frequency and N_2 is the number of cycles performed under f_2 frequency. Experimental data indicate that the fatigue life obtained by using a servo-hydraulic machine operating in a range of 10 to 50 Hz is not strongly frequency sensitive. If we set conventional operating frequency as the reference frequency $f_r = 10\ 50$ Hz, and f_p as the operating frequency under ultrasonic vibration test $f_p = 15\ 30$ kHz, then Ψ_f can be defined as $\Psi_f = f_r/f_p$, and equation (14) can be rewritten in the following form:

$$\Delta S_{\mu p} = \int_{t_0}^{t} \Psi_f \left(\phi f_v \frac{\boldsymbol{\sigma}^{\mu} : \dot{\boldsymbol{\varepsilon}}_P^{\mu}}{T} \right) dt \tag{19}$$

$$\Psi_f = \begin{cases} 1, & if\ f_p < 100\ Hz \text{ (typical servo-hydraulic machine)} \\ \dfrac{100}{f_p}, & if\ f_p \text{ is in the order of } kHz \text{ (ultrasonic vibration) or } less \end{cases} \tag{20}$$

The frequency coefficient $\Psi_f = f_r/f_p$ is used to account for the fact that at higher frequencies, more cycles are needed to reach the same volume of activated slip bands. It indicates that at a given stress amplitude, under the same number of cycles the specimen produces lower cumulative microplasticity entropy at high frequency than at low frequency, because under the same number of cycles the probability of generating microplasticity inclusions is smaller at high frequency than at low frequency. The high and low frequency mentioned here refers to the ultrasonic vibration machine and traditional servo-hydraulic machine, respectively. Equation (20) is only applicable to up to the frequency in the order of kHz because higher frequencies (e.g., MHz or UHCF that is typically above 10^7 cycles) is expected to reflect different crack initiation mechanisms and fatigue failure behavior (Marti et al., 2020; Torabian et al., 2017). Equation (20) is also applicable only for the class of materials where slip band formation dominates the crack initiation process (Marti et al., 2020; Mughrabi, 2002).

In the literature, there are other micromechanics studies of metals subject to high and very high cycle fatigue (Mughrabi, 2013; Ho et al., 2017; Mughrabi, 2009). They utilize similar micromechanics descriptions such as the following:

1. The quantitative description of cyclic irreversible slip used in the literature (Mughrabi, 2013; Ho et al., 2017), is equivalent to f_v in our formulation.
2. Cross-slip is one of the leading mechanisms in cyclic slip irreversibility, which is frequency dependent. This frequency effect is taken into account by Ψ_f (Mughrabi, 2009).

2.3. *Entropy generation due to internal atomic-friction-generated heat*

The entropy change due to internal atomic-friction (scattering)-generated heat is given by (Basaran, 2021; Basaran and Nie, 2004)

$$\Delta S_r = \int_{t_0}^{t} \frac{\rho r}{T} dt \tag{21}$$

At the atomic level, temperature is the intensity of atomic vibrations. The atomic-friction-generated heat per unit mass, r, is due to the increasing intensity of atomic vibrations in the crystal due to micro-mechanisms such as the breaking of atomic bonds, and phonon–phonon scattering, phonon-electron-scattering, electron scattering (called internal friction), (Gao, 1997; Ragab and Basaran, 2009; Chu et al., 2015), and dislocation motions. We should emphasize that this term is different than the heat generated through the macroscopic observable plastic work or thermo-elastic source.

The equation governing internal heat generation has also been derived analytically. It has been shown in the literature (De Hosson et al., 2001; Galligan et al., 2000) that the rate of internal heat generation is composed of two mechanisms: 1) the drag (friction due to scattering) process involves phonon drag, electron drag, and radiation drag (Blaschke et al., 2020; De Hosson et al., 2001; Galligan et al., 2000), and 2) the dislocation motion during the plastic deformation (Huang et al., 2008; Parvin and Kazeminezhad, 2016). The internal heat generation equation for these two mechanisms is given by,

$$\rho r^{drag} = \varrho B^{drag} v v \tag{22}$$

$$\rho r^{dis} = \frac{1}{2}\mu b^2 \dot{\varrho} - \alpha_H \mu b \sqrt{\varrho} \dot{\gamma} \tag{23}$$

where, ρ is the mass density, B^{drag} and v represents the effective drag coefficient and velocity of dislocation, respectively. The terms μ, b, ϱ, and α_H are the shear modulus, the magnitude of Burger's vector, total dislocation density, and Taylor's hardening parameter, respectively. In equation (22), the velocity of dislocation is related to the applied shear strain rate, $\dot{\gamma}$ as follows,

$$v = \frac{\dot{\gamma}}{\varrho_m b} \tag{24}$$

whereϱ_m is the density of mobile dislocations. Hence, the entropy change due to internal friction can be given by

$$\Delta S_r = \int_{t_0}^{t} \frac{\rho r}{T} dt = \int_{t_0}^{t} \frac{\left(\varrho B^{drag} v v + \frac{1}{2}\mu b^2 \dot{\varrho} - \alpha_H \mu b \sqrt{\varrho} \dot{\gamma}\right)}{T} dt \tag{25}$$

Using equation (25), the evolution of ΔS_r for the specimen under ultrasonic vibration with 400 MPa stress amplitude is shown in section 4, Fig. 4-2.

2.4. *Thermodynamic fundamental equation*

Utilizing equations (5–6), (19), (25), the thermodynamic fundamental equation can be written in the form

$$\Delta s = -\int_{t_0}^{t} \left(k_h \frac{\nabla T \bullet \nabla T}{\rho T^2}\right) dt + \int_{t_0}^{t} \Psi_f \left(\phi f_v \frac{\boldsymbol{\sigma}^{\mu} : \dot{\boldsymbol{\varepsilon}}_P^{\mu}}{\rho T}\right) dt + \int_{t_0}^{t} \frac{\left(\varrho B^{drag} v \dot{v} + \frac{1}{2}\mu b^2 \dot{\varrho} - \alpha_H \mu b \sqrt{\varrho}\, \dot{\gamma}\right)}{\rho T} dt \tag{26}$$

To be able use equations (3) and (26) to calculate the TSI evolution versus number of cycles, material parameters need to be obtained beforehand. For the microplasticity model, the Young's modulus, the hardening modulus, the Poisson's ratio, the thermal expansion coefficient, the fatigue limit (used as microscopic yield stress), and the volume fraction of activated micro-defects are necessary. For the internal friction model, the lattice and dislocation parameters are obtained from the literatures. The absolute temperature (T) in the denominator will be evaluated based on a fully-coupled thermal mechanical equation derived in section 4. 3. In order to verify the temperature simulation from the fully-coupled thermal mechanical equation, a thermographic camera is used to record the temperature profile of the specimen focusing on the gage center during fatigue loading.

3. Experimental setup and test results

The ultrasonic vibration tests were performed in the Research Laboratory of Materials and Constructions at the Faculty of Mechanical Engineering in the University of Science and Technology in Bydgoszcz, Poland. The laboratory is accredited by the Polish Centre for Accreditation (PCA AB 372) in compliance with ISO/IEC 17025:2018-02 and the accreditation covers, among others, most of the testing methods described in this section.

Specimens for all tests described in this section were made of non-alloy quality structural steel (EN numeric designation: 1.0577, EN chemical designation: S355J2 + N, equivalent grade in the USA: A656

Table 3.1
The content of main components of 1.0577 steel (wt. %).

Standard composition	C	Si	Mn	P	S	Cu
According to EN 10025–2-2004	max 0.20	max 0.55	max 1.60	max 0.03	max 0.03	max 0.55
Tested specimen	0.12	0.19	1.29	0.004	0.015	0.20

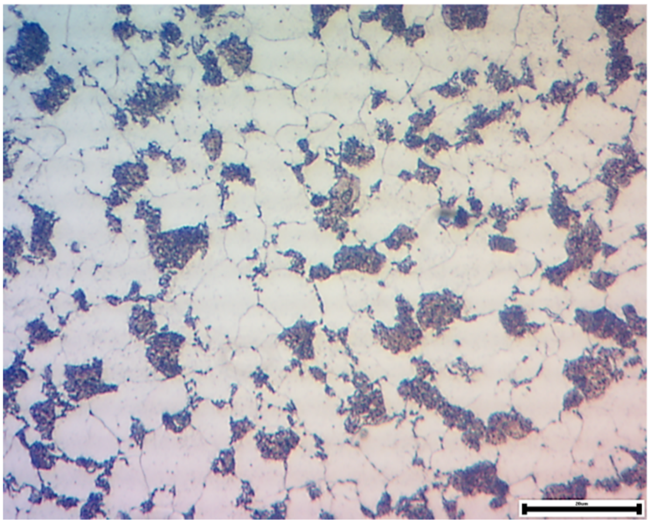

Fig. 3-1. Microstructure after normalization (marked line segment has 20 μm length).

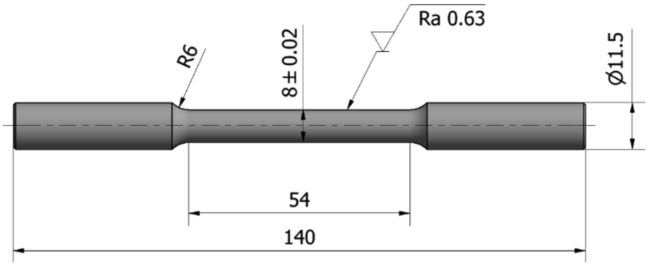

Fig. 3-2. Main dimensions of the specimens used for tensile strength tests, (unit, mm).

grade) provided in the form of a drawn round bar with a diameter of Ø12 h9 with surface roughness class 3 (parameter R_a max 20 μm). The density of this material is 7820 kg/m^3. The chemical composition of the tested material is shown in Table 3.1.

The round bars were normalized before specimen preparation. Heating was carried out in a vacuum furnace; the annealing temperature was between 920 °C and 940 °C and the annealing duration was 80 min. Cooling after annealing was done in the air. The microstructure of the material after normalizing (annealing process) is presented in Fig. 3-1. The microstructure consists of ferrite (bright particles) and pearlite (dark particles.)

3.1. Tensile testing

The tests were carried out at room temperature in accordance with the standard PN-EN ISO 6892–1:2020–05 using the servohydraulic testing machine INSTRON 8502 fitted with the control system 8500+. The main parameters of the testing machine: maximum static force – 300 kN, maximum dynamic force – 250 kN, piston stroke - ±75 mm. The specimens (Fig. 3-2) were also tested in uniaxial monotonically increasing tension up to their failure. The load and the displacement of the test machine, together with the strain in the sample, were recorded during tests using the INSTRON 2630–113 extensometer with the measurement base of 50 mm and the measuring range from −5 to + 50 mm. The tests were carried out with displacement control at the speed of 0.05 mm/s.

One of many stress–strain curves obtained by tensile tests is given in Fig. 3-3. The tensile properties obtained by tests are shown in Table 3.2.

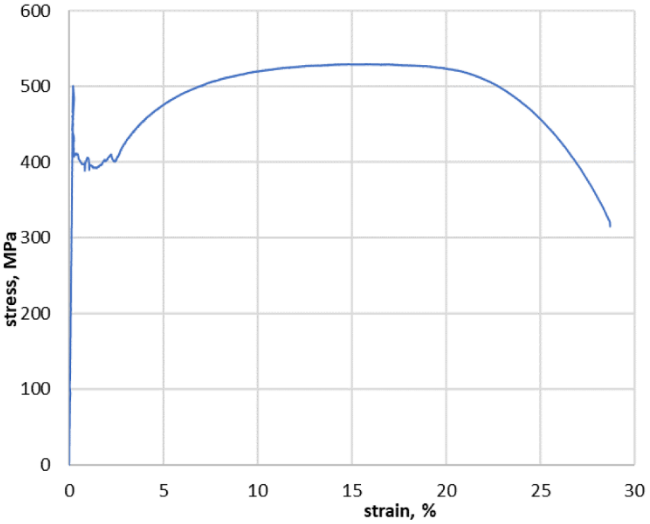

Fig. 3-3. Engineering stress–strain curve obtained by tensile test.

Table 3.2
Main tensile properties of 1.0577 steel.

Upper Yield Strength R_{eH} (UYS)	498 MPa
Lower Yield Strength R_{eL} (LYS)	400 MPa
Ultimate Tensile Strength R_m (UTS)	529 MPa

3.2. Young's modulus

The tests were carried out at room temperature in accordance with the standard PN-EN ISO 6892–1:2020–05 using the servohydraulic testing machine INSTRON 8502 fitted with the control system 8500+. During tests, the specimen (Ø12 round bar) was subjected to uniaxial monotonically increasing tension up to 250 MPa (approx. 50% of R_{eH} = 498 MPa) of nominal stress with a stress rate of 30 MPa/s. The load and the displacement of the test machine, together with the longitudinal strain in the sample, were recorded during tests using the INSTRON 2620-603 extensometer with a measurement base of 50 mm and the measuring range of ±1 mm. Regression analysis was used for the data in the range of:

- lower stress value: $R_1 = 10\%$ of $R_{eH} = 49.8$ MPa,
- upper stress value: $R_2 = 40\%$ of $R_{eH} = 199.2$ MPa.

The Young's modulus was specified as follows:

$$E = \frac{\sigma}{\varepsilon} \tag{27}$$

where: E - modulus of elasticity, MPa, σ - nominal stress, MPa, ε - longitudinal strain measured by extensometer, mm/mm. The Young's modulus is the slope of $\sigma = f(\varepsilon)$ curve obtained by linear regression and is calculated to be $E = 197\,265$ MPa. Based on this value and the tensile test results, the hardening modulus was determined as $H = 879$ MPa. H is defined as the slope between (lower yielding strength) LYS and UTS (ultimate tensile strength). We use this hardening modulus in the linear kinematic hardening rule, eq (13).

In addition to this test in room temperature, the Young's modulus was also determined for the range of from 50 °C to 175 °C with an incremental step of 25 °C. In this range, the change in the Young's modulus value was less than measurement uncertainty (about 3.5%) and it can be assumed that it is a constant value in the range up to 175 °C. Above this temperature, the Young's modulus decreases significantly (over 11% for temperature 225 °C and 20% for 450 °C).

Fig. 3-4. Longitudinal and transverse extensometers on the specimen for Poisson's ratio determination.

3.3. Poisson's ratio

Simultaneously, with the measurement of the longitudinal strain to determine the Young's modulus, the value of transverse strain was also measured by the INSTRON 2640–007 transverse extensometer with the measuring range of 0.5 mm (Fig. 3-4).

The test conditions and data range for Poisson's ratio determination were the same as for Young's modulus. The Poisson's ratio was specified as follows:

$$\nu = -\frac{\varepsilon_{trans}}{\varepsilon_{long}} \tag{28}$$

where: ν - Poisson's ratio, ε_{trans} - strain measured by transverse extensometer, mm/mm, ε_{long} - strain measured by longitudinal extensometer, mm/mm. The Poisson's ratio is the slope of $\varepsilon_{trans} = f(\varepsilon_{long})$ curve obtained by linear regression and is $\nu = 0.27$.

3.4. Thermal expansion coefficient

The test was performed using Instron 3-zone CT-SF/770 heating split furnace with a maximum temperature of +1000 °C and a computer temperature control system. The specimen temperature was measured by thermocouple TP-203 with an EMT-200 temperature meter. The specimen strain was measured by an extensometer designed for high temperatures.

The specimen was heated from 25.2 °C to the next level, at which the temperature was stabilized and the strain was read. The maximum temperature was 156.7 °C. The thermal expansion coefficient was specified as follows:

$$\alpha = \frac{\varepsilon}{\Delta T} \tag{29}$$

where: α is thermal expansion coefficient, 1/K, ε is strain measured by extensometer, mm/mm, ΔT is temperature increase in relation to the initial temperature of 25.2 °C, °C. The thermal expansion coefficient is the slope of $\varepsilon = f(\Delta T)$ curve obtained by linear regression and is $\alpha = 12.6 \cdot 10^{-6}$ 1/K in the range of temperature from 25 °C to 150 °C.

3.5. Modal analysis with FEM

Ultrasonic vibration fatigue test is carried out in the resonance frequency of the sample in the axial direction (Bathias and Paris, 2005; Freitas et al., 2011). Therefore, modal analysis is necessary to determine the natural frequencies of the tested specimen. In order to calculate the natural frequencies of the test specimen, a simple undamped finite element model in Abaqus FEM software (Linear perturbation analysis steps (General and perturbation procedures, 2021) was performed. The sample presented in Fig. 3-5 is a standard specimen used for very high cycle fatigue (VHCF) tests for steel.

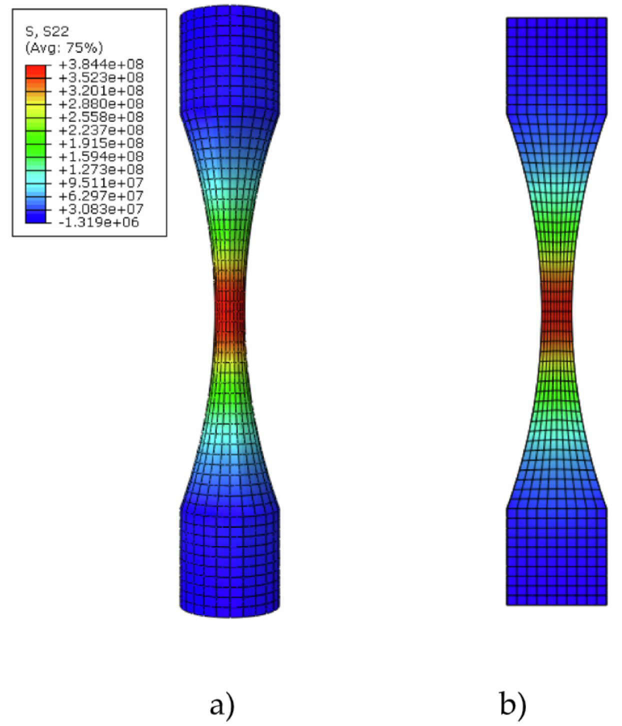

Fig. 3-5. Normal stress distribution in the axis direction of the specimen a) on the surface b) in its longitudinal cross-section. For average stress of σ = 380 MPa.

First, the value of the tension–compression resonance frequency in the axial direction was determined to be 19,864 Hz.

Then, for the resonance frequency, the stress distributions were determined for selected levels of the vibration amplitude of the end of the sample. A linear relationship between the vibration amplitude and the average stress in the centre of the sample was determined as,

$$\sigma = 20,510 \bullet A$$

where: σ is the average normal stress in the centre of the sample in MPa, A is the vibration amplitude in mm. The stress is greater on the surface of the specimen and smaller in the centre. These stresses are in the range of about ± 1% of the average stress in the narrow gauge section.

Fig. 3-5 shows the stress distribution in the axial direction of the specimen axis on the surface and in its longitudinal cross-section for average stress $\sigma = 380$ MPa ($A = 0.0185$ mm). Stress and displacement distribution along the specimen axis for σ = 380MPais presented in Fig. 3-6.

3.6. Determination of fatigue limit

The fatigue tests included two types of experiments:

- determination of fatigue limit (Up-And-Down Method),
- determination of high-cycle fatigue curve.

Each test was carried out independently on different number of samples.

Samples were used for determination of fatigue limit. Among these

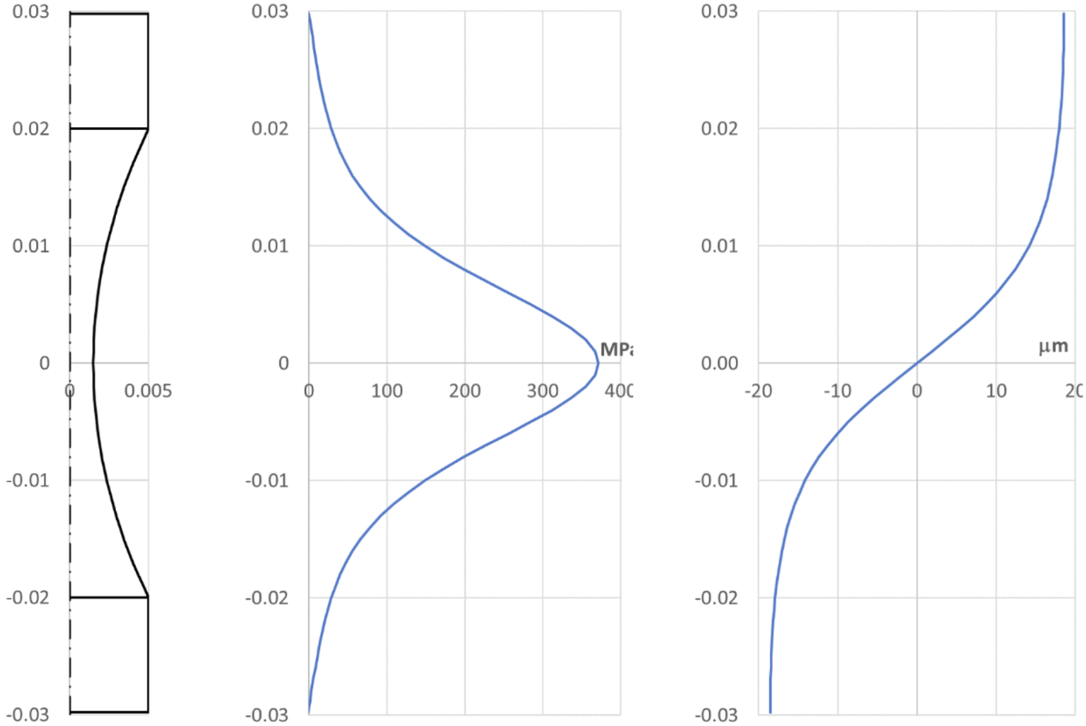

a) b) c)

Fig. 3-6. Sample dimensions along the axis, b) Stress distribution along the sample c) displacement distribution along the specimen axis for average stress of $\sigma = 380$ MPa.

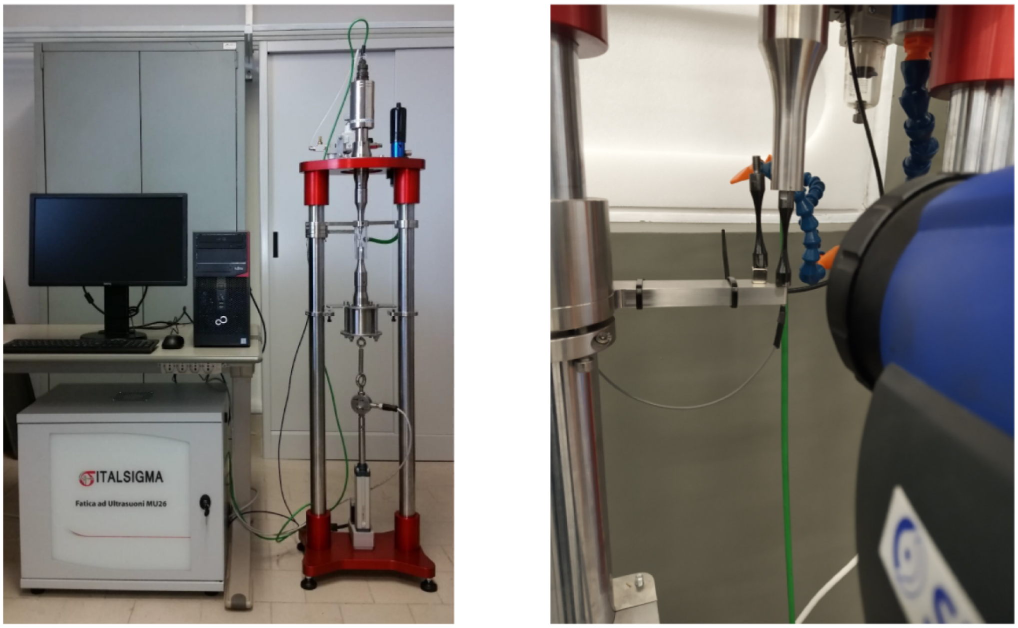

a) b)

Fig. 3-7. a) Ultrasonic resonance testing machine ItalSIGMA MU26 b) tested and reference specimens for IR thermography.

21 samples, 10 samples failed, 11 samples did not unfail.

15 samples were used to determine the high-cycle fatigue curve. All 15 samples failed. For the temperature monitoring during the fatigue tests, 11 samples were observed using IR camera. Hence only 11 profiles are shown in Fig. 3-11.

All fatigue tests described in this section were performed on ultrasonic resonance testing machine ItalSIGMA MU26 (Fig. 3-7a) with a stress ratio of $R = -1$ (Note: it is possible to test at $R > -1$). The testing system generates harmonic sinusoidal longitudinal vibrations with a frequency of 20 ± 0.5 kHz and with a maximum vibration amplitude of

60 μm. During tests, the thermographic camera CEDIP Silver 420 M (FLIR SC5200) equipped with high sensitivity InSb matrix cooled using a Stirling pump recorded, [at a constant frequency of 25 Hz], the surface temperature distribution of the specimen fixed in the testing machine (Fig. 3-7b). A second reference specimen was used to monitor the influence of the environment on the temperature of the loaded sample. Main parameters of the camera: resolution of sensor 320 × 256 pixels, spectral range 3.6 ÷ 5.0 μm, sensitivity below 20 mK, maximum frequency 140 Hz for the entire matrix. Processing of thermographic images recorded by the camera was made by using ALTAIR and MATLAB software.

The fatigue limit has been determined using the Staircase (Up-And-Down) Method (Chrysochoos et al., 2012). 21 samples (Fig. 3-8) were tested to ten million cycles. The initial stress level in the test was 360 MPa and the load step was 10 MPa (Fig. 3-9).

The Dixon-Mood (Dixon and Mood, 1948) formula was used to calculate the mean and the standard deviation of the fatigue limit based on the results of the Up-And-Down method (Dixon, 1965). Assuming a 95% confidence level, the fatigue limit is determined to be 368 ± 3.3 MPa.

3.7. Fatigue data

A very high-cycle fatigue S-N curve has been determined for the stress ratio of $R = -1$ using the same ultrasonic testing system described earlier (Fig. 3–7) and specimens shown in (Fig. 3–8) as in the case of fatigue limit determination. The fatigue test data obtained from 15 failed specimens tested in a range of stresses between 360 MPa and 400 MPa with 95% confidence intervals is shown in (Fig. 3-10).

The Basquin's relation described fatigue curve is:

$$S_a^m \cdot \mathrm{N} = \mathrm{C}, \tag{30}$$

where: S_a is stress amplitude, MPa, N is fatigue life in cycles, m, C are exponent and constant, respectively, in Basquin's relation. In this case $m = 9.8$ and $C = 9.7 \cdot 10^{31}$.

During tests, the surface temperature distribution of the specimen was recorded by a thermographic camera. The surface temperature at the gage center of the sample, T, versus the number of cycles for different constant amplitude load levels, S_a, is shown in Fig 3-11. The temperature undergoes three phases: rapid growth at the beginning of the loading (phase 1), parabolic [approximately linear] growth in the middle (phase 2), and rapid temperature rise associated with the appearance of a macro crack (phase 3) [our approach is borrowed from the technique used in identifying stages of creep in metals, primary, secondary and tertiary creep]. The temperature in phase 2 did not exceed 400 K. When a macro crack appears in phase 3, a rapid increase in temperature was noticed, reaching an instantaneous value of up to 440 K. Fig. 3-12a-d are the thermograms of the specimen that show the surface temperature distribution of the specimen in different phases under 400 MPa stress amplitude.

It is shown that a temperature gradient between specimen's gage section and grip section increases slowly in phase 2, and then rises rapidly when a microcrack forms, phase 3.

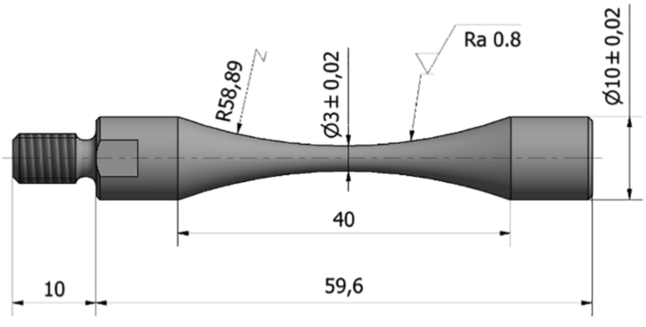

Fig. 3-8. Dimensions (in mm) of the specimens used for ultrasonic fatigue tests.

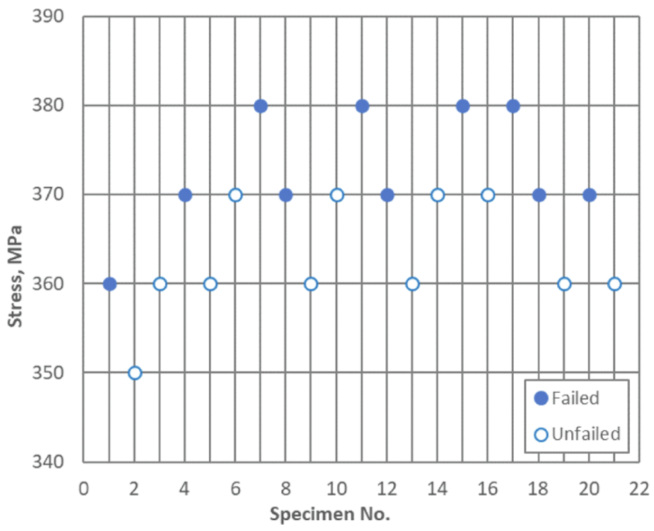

Fig. 3-9. Staircase fatigue data for 21 samples that undergo the fatigue limit test using the Up-And-Down Method. Among these samples, 10 samples failed, 11 samples did not fail.

3.8. Fractography images

Fracture surface images obtained by SEM are presented in Fig. 3-13. These surfaces consist of two areas. The smooth annular area [in the dark region] around the outer side is the fractured/separated area, due to the fatigue load. Fatigue fracture in this area caused a change in the geometry of the sample, and thus the test was stopped. Because the resonance frequency of the sample changed significantly after a macro crack developed, the testing setup lost the ability to maintain resonance in the sample. This sometimes happened without complete separation of the specimen into two pieces. The core located in the center is a plastically deformed area as a result of breaking the sample by monotonic tension after the loss of resonance during the fatigue test, [when the sample did not break into two pieces on its own]

4. Entropy and thermodynamic state index (TSI) calculation

Before applying equation (3) and (26) to calculate the entropy change and TSI evolution versus cycles. It is helpful to present the required material parameters collected from section 3 experiments and literatures. The derivation of the absolute temperature T in equation (6), (19), (25) and (26) based on a fully coupled thermal mechanical equation is also evident for the calculation of entropy and TSI evolution.

4.1. Material constants for micro-plasticity calculation

In order to compute the entropy change due to microplasticity material properties need to be defined. These material constants obtained from section 3 are collected in Table 4.1.

The microscopic yield stress is the mean fatigue limit of the specimen, it is assumed that no microplasticity occurs below the macroscopic fatigue limit, Lemaitre et al (Lemaitre et al., 1999).

It should be noted that the microplasticity calculation in this subsection is based on the following assumptions:

1. The hardening behavior of the material is approximated by a bilinear kinematic hardening. Hardening modulus is defined as the slope between (lower yielding strength) LYS and UTS (ultimate tensile strength) from the test stress–strain curve, as a first approximation.

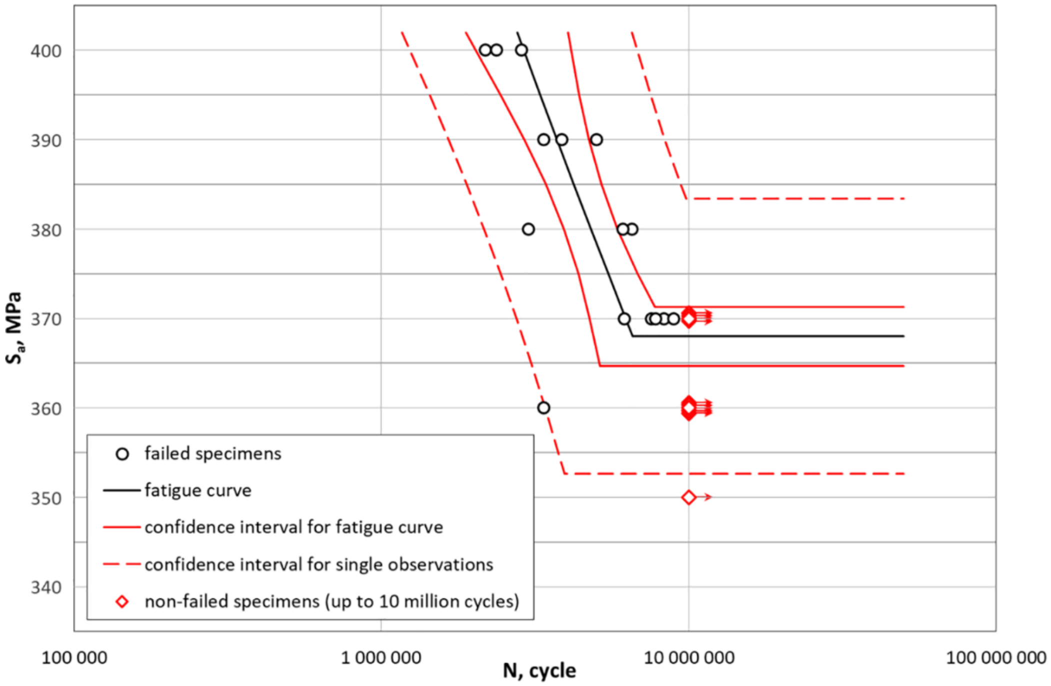

Fig. 3-10. Fatigue data for 15 samples, as stress versus number of cycles to failure. All 15 samples were failed.

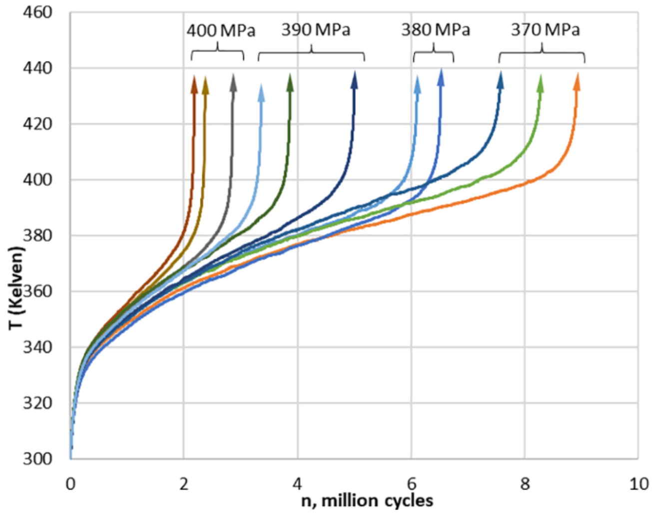

Fig. 3-11. Surface temperature at the gage center of the 11 monitored samples versus number of cycles (in millions) during the fatigue tests.

2. The microscopic hysteresis loops are stabilized and they are the same at each defect site. The evolution of TSI, ϕ, from 0 to 1 only induces microplasticity at more defect sites.

The entropy change due to microplasticity calculated by equation (19–20) is shown in Fig 4-2.

4.2. *Material constants for internal friction calculation*

It has been shown that during the deformation of iron and iron alloys, the proportion of the main types of dislocations are approximately 60% of $\frac{1}{2}\langle 1\ 1\ 1\rangle$, 20% of $\langle 1\ 0\ 0\rangle$, and 20% of $\langle 1\ 1\ 0\rangle$, which are unaffected by temperature of deformation, alloy content, amount of strain, dislocation density or rate of straining (Bergström et al., 2010). The magnitude of the burgers vectors can be calculated by,

$$\|\boldsymbol{b}\| = \left(\frac{a}{2}\right)\sqrt{h^2+k^2+l^2} \quad \text{For BCC and FCC lattice} \tag{31}$$

$\|\boldsymbol{b}\| = (a)\sqrt{h^2+k^2+l^2}$For simple cubic latticewhere $\|\boldsymbol{b}\|$ is the magnitude of the burgers vector, a is the lattice constants in units of angstrom(Å), and h, k, l are the components of the burgers vector.

The parameters in equation (22–24) can be obtained by discrete dislocation dynamics. However, we use values reported in literature for the same material, as follows

)1. The burgers vector values from reference (Bergström et al., 2010) is used. The terms related to burgers vector are summed according to their proportion.

)2. Taylor's hardening parameter α_H is a dimensionless parameter ranging from 0.05 to 2.6 used to characterize the burger's relation between the flow stress of a material to its dislocation density, $\tau = \tau_0 + \alpha\mu b\sqrt{\rho}$, (Davoudi and Vlassak, 2018; Jamal et al., 2021). We use the Taylor's parameter from reference (Jamal et al., 2021) that gives a similar stress–strain curve as our material.

)3. The initial dislocation density value for a mild steel is used from reference (Blaschke, 2019).

)4. Moving dislocations experience a drag due to their interaction with the crystal structure, and this drag coefficient B^{drag}determines the dislocation glide time between obstacles (Blaschke et al., 2019; Messerschmidt and Bartsch, 2003). If drag mechanism is considered, we assume the phonons scattering off dislocations constitutes the dominating effect, and the B^{drag} from reference (Blaschke et al., 2019) is used.

)5. The evolution of dislocation density during plastic deformation has been extensively studied in the literature (Voyiadjis and Abed, 2005; Viatkina et al., 2007; Huang et al., 2008; Shanthraj and Zikry, 2011; He et al., 2018; Guo et al., 2015). The literature concluded that the increase of total dislocation density that compose of dislocation generation and annihilation is related to the increasing plastic deformation (Shanthraj and Zikry, 2011; He et al., 2018; Guo et al., 2015). In our study nominal macro stress is well below the yield stress, and the micro-plastic deformation

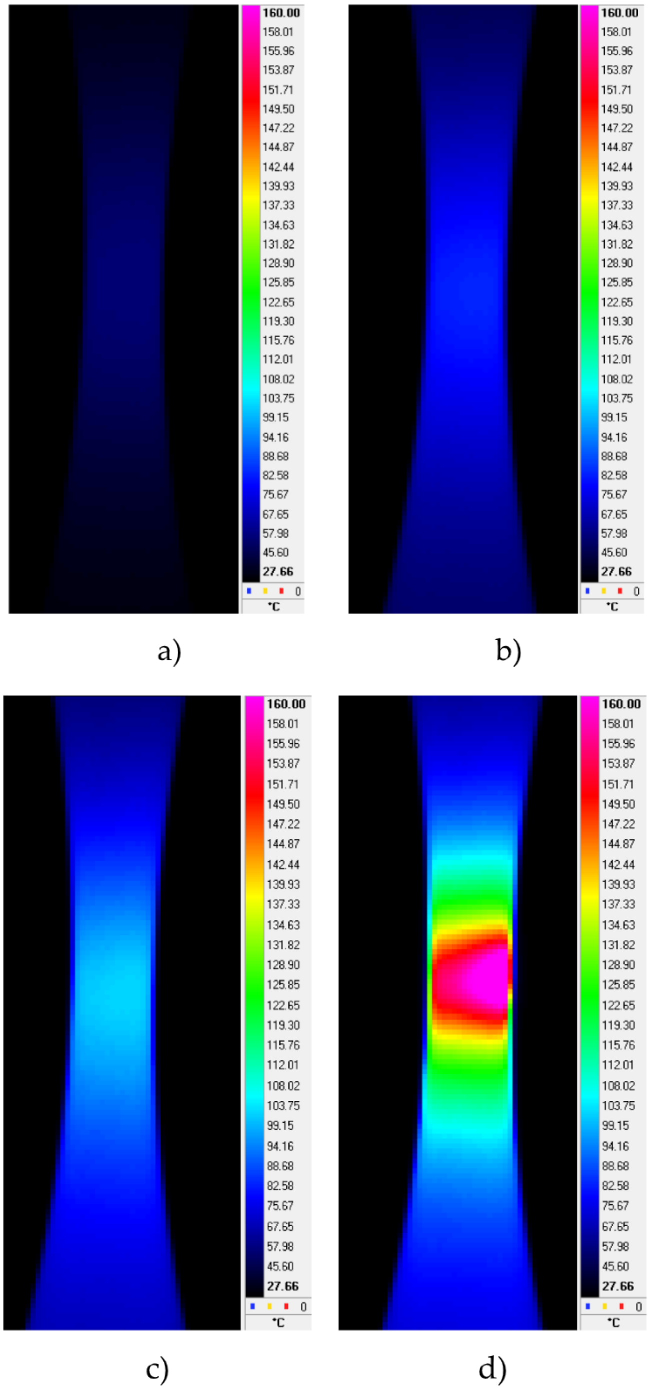

a) b)

c) d)

Fig. 3-12. Temperature distribution on the surface of the specimen at a) end of phase 1, b) middle of phase 2, c) end of phase 2, d) end of phase 3 (start of cracking). For stress amplitude of $\sigma = 400$ MPa.

that result in stabilized hysteresis micro stress–strain loops only happens at micro defects sites, which evolve with thermodynamic state index. Therefore, we assume a constant dislocation generation rate $\Delta\varrho$ at each defects site, and the total contribution from dislocation motions (equation (22–23)) increases as the thermodynamic state index ϕ evolve towards one, as a first approximation.

The parameters appear in equation (22–24) are summarized in the following table:

Using the above assumptions and parameters given Table 4.2, the entropy change due to internal frictions calculated by equation (25), is shown in Fig 4-2.

4.3. Fully-coupled thermo-mechanical equation

The absolute temperature T in the denominator of equation (6), (19), (25) and (26) is governed by the fully-coupled thermo-mechanical equation derived from classical continuum mechanics as follows, (Basaran, 2021; Basaran and Nie, 2004):

$$\rho c_V \dot{T} - k\nabla^2 T = \boldsymbol{\sigma} : \dot{\boldsymbol{\varepsilon}}^p + T\left(\frac{\partial \boldsymbol{\sigma}}{\partial T} : \dot{\boldsymbol{\varepsilon}}^e\right) + \rho r + T\left(A_k - \frac{\partial A_k}{\partial T}\right)\dot{V}_k \tag{32}$$

In which the first term is the rate of heat storage, the second term is the heat conduction, the third term is the energy dissipation due to macro plastic work, the fourth term is the thermoelastic coupling source, the fifth term is the heat generation due to internal frictions, and the last term is non-recoverable energy corresponding to the internal coupling source. In equation (32), $c_V = T\frac{\partial s}{\partial T}$ is defined as specific heat capacity, $\boldsymbol{\varepsilon}^e$ and $\boldsymbol{\varepsilon}^p$ are elastic and plastic strain tensors, respectively, $\boldsymbol{\sigma}$ is the stress tensor, $\boldsymbol{r}$ is the strength per unit mass of the internal distributed heat generation, and A_k is a thermodynamic force associated with the internal thermodynamic variables, V_k.

Equation (32) can yield the evolution of temperature due to mechanical work with properly imposed boundary conditions. In order to simplify this equation, we can ignore plastic strain $\dot{\boldsymbol{\varepsilon}}^p$, and other thermodynamic variables $A_k\dot{V}_k$.

These assumptions are valid, because,

1. We are investigating mechanical response under elastic loads only, as such there is no uniform plastic strain. However, the contribution from microplasticity is not neglected.
2. $\left(A_k - T\frac{\partial A_k}{\partial T}\right)\dot{V}_k$ represents the non-recoverable energy corresponding to the internal coupling source (e.g., sound waves, grain coarsening, phase transformation, etc.). However, for metals this non-recoverable energy only represents 5% of the total dissipation, (Teng et al., 2020; Naderi et al., 2009).

Hence, utilizing equations (22–23) and two assumptions stated above, equation (32) can be rewritten in to the following expression

$$\rho c_V \dot{T} - k\nabla^2 T = \Psi_f\left[\phi f_v\left(\boldsymbol{\sigma}^\mu : \dot{\boldsymbol{\varepsilon}}_P^\mu\right)\right] + \varrho B^{drag} v v + \frac{1}{2}\mu b^2 \dot{\varrho} - \alpha_H \mu b \sqrt{\varrho}\dot{\gamma} \tag{33}$$

where, ρ is the mass density, B^{drag} and v represents the effective dislocation-drag coefficient and velocity of dislocation, respectively. The terms, k_h, ϕ and c_V are coefficient of heat conduction, the thermodynamic state index and the specific heat capacity, respectively. The relative surface ratio covered by activated micro slip bands is represented by f_v. The terms μ, b, ϱ, and α_H are the shear modulus of the bulk material, the magnitude of Burger's vector, total dislocation density, and Taylor's hardening coefficient, respectively.

In equation (33), the term, $k_h\nabla^2 T$ represents the heat conduction. If we ignore the thermal fluctuation due to thermo-elastic dissipation and assume that the temperature field is uniform, we can simplify the conduction term as $-k_h\nabla^2 T \cong \rho c_V \frac{\theta}{\tau_{eq}}$ (Torabian et al., 2017).

Where, the terms, θ and τ_{eq} are the total change in temperature $(T_n - T_0)$ and a conduction time constant used to characterize the heat transfer between the specimen and the surroundings (Charkaluk and Constantinescu, 2009; Zhang et al., 2013; Dingley and Hale, 1966).

Then, the following equation is obtained

$$\rho c_V\left(\dot{T} + \frac{(T_n - T_0)}{\tau_{eq}}\right) = \Psi_f\left[\phi f_v\left(\boldsymbol{\sigma}^\mu : \dot{\boldsymbol{\varepsilon}}_P^\mu\right)\right] + \varrho B^{drag} v.v + \frac{1}{2}\mu b^2 \dot{\varrho} - \alpha_H \mu b \sqrt{\varrho}\dot{\gamma} \tag{34}$$

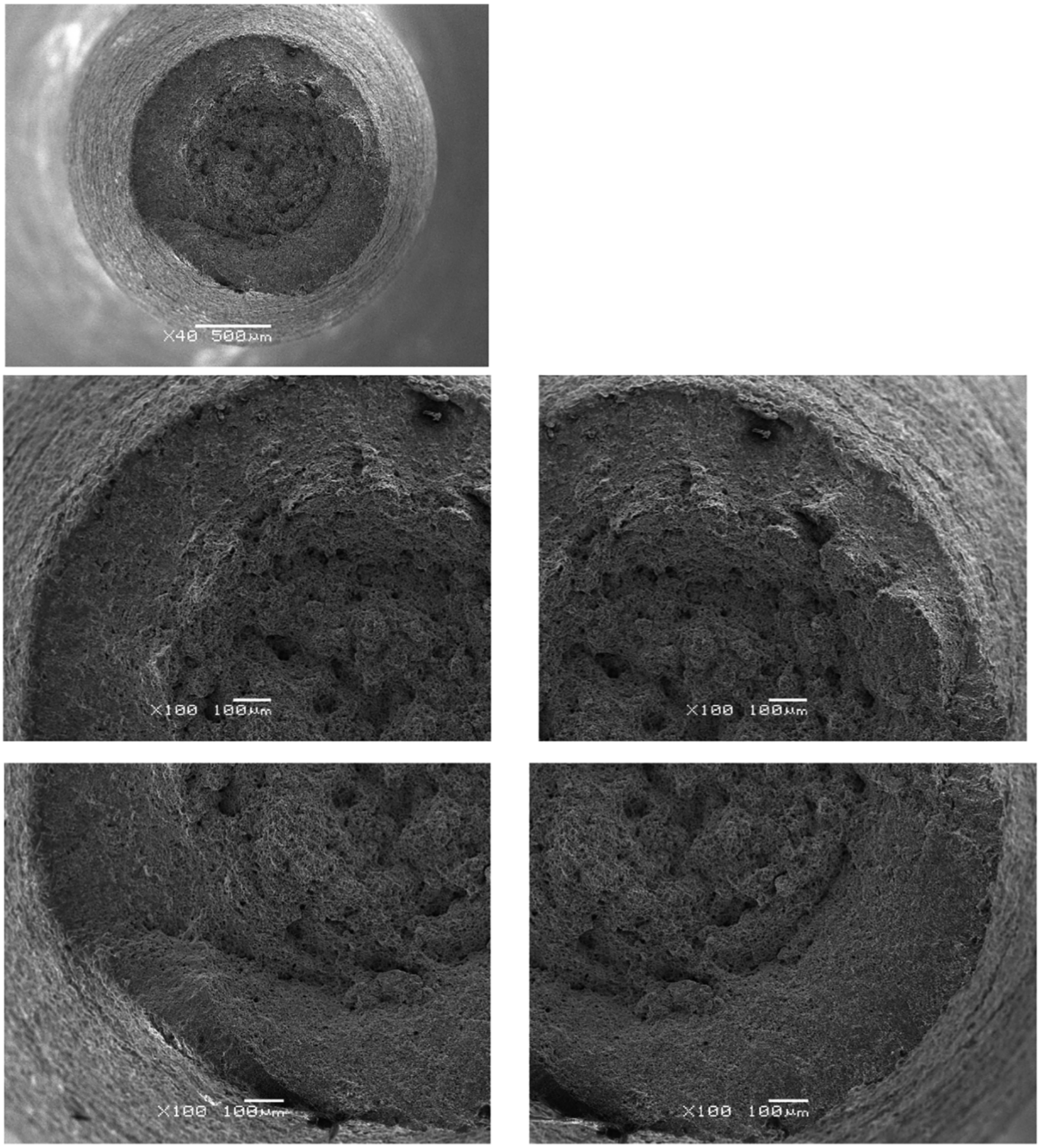

Fig. 3-13. Sample SEM images of the fracture surfaces for load level 400 MPa.

Table 4.1
Material parameters for EN 1.0577 steel.

Youngs modulus	197265 MPa	Macroscopic yield stress	400 MPa
Hardening coefficient	879 MPa	Microscopic yield stress	368 ± 3.3 MPa
Poisson's ratio	0.27	Thermal expansion coefficient	$12.6 \cdot 10^{-6}$ K^{-1}
Density	7820 Kg m^{-3}	Specific heat capacityc_V	470 J $Kg^{-1}K^{-1}$
Volume fraction of inclusionsf_v	20%	Frequency coefficient Ψ_f from eq (24) using$100/f_p$	$5 \cdot 10^{-3}$
Critical thermodynamic index	$\phi_{cr} = 0.97$		

Table 4.2
Parameters used in the proposed model for mild steel.

Parameter	Symbol	Value	Units
Lattice constants	a	2.856	$10^{-10}m$
Magnitude of burgers vector	b	60%of 0.87a 20% of 1.00a 20% of1.41a	angstrom
Shear modulus	μ	7.76×10^4	MPa
Taylor's hardening parameter	α_H	1	–
Initial dislocation density	ϱ	0.88×10^{14}	m/m^3
Drag coefficient due to transverse phonon drag	B^{drag}	0.02	mPa-sec
Dislocation density increment in each cycle	$\Delta\varrho$	1.523×10^{14}	m/m^3

The time discretization of the above equation is given by,

$$\Delta T_{n+1} = -\frac{\Delta t}{\tau_{eq}}(T_n - T_0) + \frac{\Delta t}{\rho c_V}\Psi_f\left[\phi f_v\left(\boldsymbol{\sigma}^{\mu} : \dot{\boldsymbol{\varepsilon}}_P^{\mu}\right)\right] + \frac{\Delta t}{\rho c_V}\varrho B^{drag}\left(\frac{\dot{\gamma}_p^{\mu} n+1}{\varrho_m b}\right)^2 + \frac{\Delta t}{\rho c_V}\frac{1}{2}\mu b^2\frac{\Delta\varrho_{n+1}}{\Delta t} - \frac{\Delta t}{\rho c_V}\alpha_H \mu b\sqrt{\varrho}\dot{\gamma} = 0 \tag{35}$$

After rearranging the terms in Eq. (35), we get the following equation for calculating the change in temperature,

$$\Delta T_{n+1} = -\ell_{eq}(T_n - T_0) + \frac{\Psi_f}{\rho c_V}\left[\phi f_v\left(\sigma^{\mu}{}_{n+1}\dot{\varepsilon}_P^{\mu}\right)\right]\Delta t + \frac{1}{\rho c_V}\varrho B^{drag}\left(\frac{\dot{\gamma}_p^{\mu} n+1}{\varrho_m b}\right)^2 \Delta t$$

$$+\frac{1}{\rho c_V}\frac{1}{2}\mu b^2\Delta\varrho_{n+1} - \frac{1}{\rho c_V}\alpha_H\mu b\sqrt{\varrho}\dot{\gamma}_p^{\mu}\Delta t \tag{36}$$

In Eq. (36) we define a dimensionless time factor, $\ell_{eq} = \frac{\Delta t}{\tau_{eq}}$. This coefficient represents the fraction of heat conducted. In this study we used the τ_{eq} value measured and reported by Charkaluk and Constantinescu [2009].

Temperature evolution in the material is calculated at each cycle using equation (36). It should be emphasized that equation (36) is primarily used to simulate the phase 1 and phase 2 temperature evolution. It will not capture the abrupt temperature rise in phase 3 when a macro crack initiates because the mechanisms for macro-plasticity, crack formation and propagation are not included.

Fig. 4-1 shows the surface temperature at gage center versus number of cycles based on equation (36).

4.4. *Temperature and entropy calculation*

The entropy change due to heat conduction, microplasticity and internal frictions during phase 1 and phase 2 are obtained directly from physics without any curve fitting. The temperature rise during phase 1 (shown in Fig. 4-1, up to 2.5x 10^5 cycles) matches the test data shown in Fig 3-11. Some researchers in the literature reported this rate ΔT_{phase1} to be a constant value, (Xue et al., 2007), analogous to the elastic modulus of a material. The temperature rise during phase 2 has a parabolic temperature increase due to microplastic work and local heat loss. The simulation values shown in Fig. 4-1 are compared with test data shown in Fig 3-11, before the onset of phase 3. At the end of phase 2 there is a small difference with test data. We believe that this discrepancy may be due to the uncertainty of the formation of cross-slip mechanisms [which leads to microplasticity], introduced by the frequency effects. However, the difference between the simulation and measured temperature values is very small for all practical purposes.

Fig 4-2 shows that the entropy generation due to microplasticity is small in the beginning of loading and starts to increase after a certain threshold. This is because there are very few activated micro defects at the initial reference state [$\phi \approx 0$]. As more micro defects are activated, more entropy is produced.

4.5. *Comparison between different entropy generation mechanisms*

The order of magnitude of each entropy generation mechanism is summarized in Table 4.3.

From Table 4.3, It is observed that during ultrasonic vibration very high cycle fatigue, the entropy generation due to thermal conduction, atomic friction generated heat, and microplasticity are about at the same order of magnitude. Still, microplasticity is the main contributor. Hence none of these three mechanisms should be ignored. The thermodynamic state index can then be given by

$$\phi = \phi_{cr}\left[1 - \exp\left(\frac{m_s\left(\int_{t0}^{t}\left(k_h\frac{\nabla T \bullet \nabla T}{T^2}\right)dt - \int_{t0}^{t}\frac{(B^{drag}v\dot{v} + \frac{1}{2}\mu b^2\dot{\varrho} - \alpha_H\mu b\sqrt{\varrho}\,\dot{\gamma})}{T}dt - \int_{t0}^{t}\Psi_f\left(\phi f_v\frac{\boldsymbol{\sigma}^{\mu} : \dot{\boldsymbol{\varepsilon}}_P^{\mu}}{T}\right)dt\right)}{\rho R}\right)\right] \tag{37}$$

Of course, equation (37) is exponential and the TSI never reaches unity. In practice we determine a ϕ_{cr} as a threshold. In this paper, we consider the specimen is failed when ϕ reaches $\phi_{cr} = 0.97$, since the probability of reaching maximum entropy at this state is 97%. We believe this value provides sufficient precision.

4.6. *TSI evolution*

The calculation of TSI requires a summation of the entropy generation due to all mechanisms. The material properties necessary for calculating TSI are presented in Tables 4.1 and 4.2. As mentioned in section 3, the material properties in Table 4.1 can be regarded as constant between 25 °C and 150 °C. From Fig 3-11 we can also observe that the temperature evolution in the specimen under ultrasonic vibration test never exceeds 130 °C (around 400 K) before rapid temperature growth at phase 3 when a macro crack initiates. Therefore, we can use the above constants for simulation without a temperature correction. For the material parameters in Table 4.2, we use the same assumption.

Using equation (37), we can compute the TSI evolution for EN 1.0577 steel operating at 20 kHz. The entropy generation and TSI variation for different stress amplitudes are presented in Fig. 4-3 and Fig. 4-4, respectively. Fig. 4-3 shows that Fatigue Fracture Entropy (FFE) is the same regardless of the stress level during testing. This is similar to results reported earlier, (Naderi et al., 2009; Yun and Modarres, 2019). The cumulative specific entropy production at failure [fatigue fracture entropy or FFE] is validated to be a material constant independent of stress amplitude, specimen's dimension and geometry, and loading

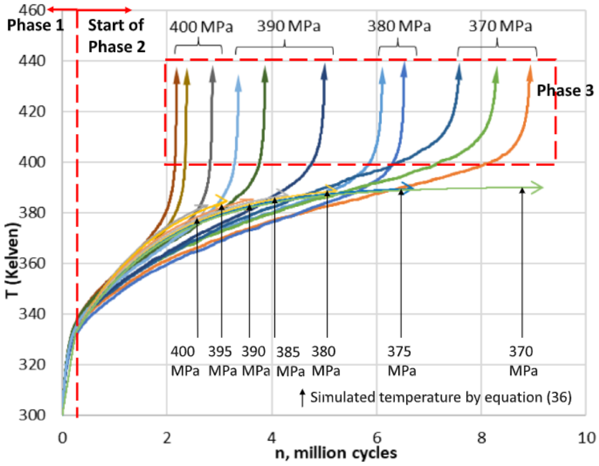

Fig. 4-1. Surface temperature at gage center versus number of cycles under various stress amplitude based on equation (36). Compared to test data (Fig. 3-11).

Table 4.3
Order of magnitude of different entropy generation mechanisms.

	Mechanism	Magnitude of entropy generation
1	Thermal conduction	$\approx 0.25\mathrm{MJK^{-1}m^{-3}}$
2	Internal friction	$\approx 0.85\mathrm{MJK^{-1}m^{-3}}$
3	Microplasticity	$\approx 3\mathrm{MJK^{-1}m^{-3}}$

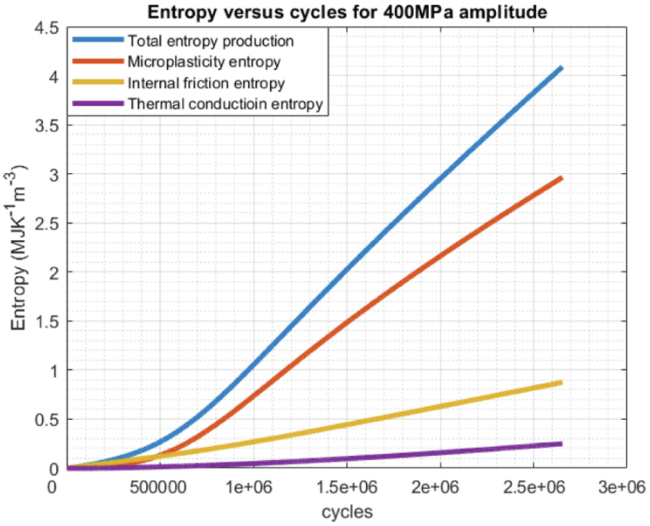

Fig. 4-2. Total entropy generation ($\mathrm{MJK^{-1}m^{-3}}$) due to various mechanisms versus number of cycles under 400 MPa nominal stress amplitude.

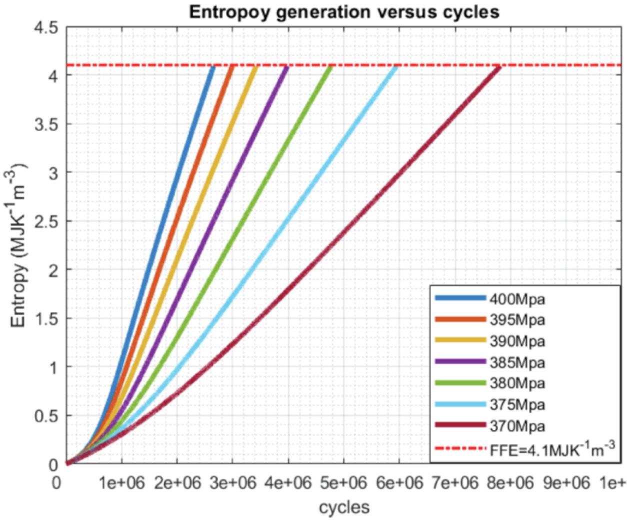

Fig. 4-3. Entropy generation versus cycles for 1.0577 steel under various stress amplitudes.

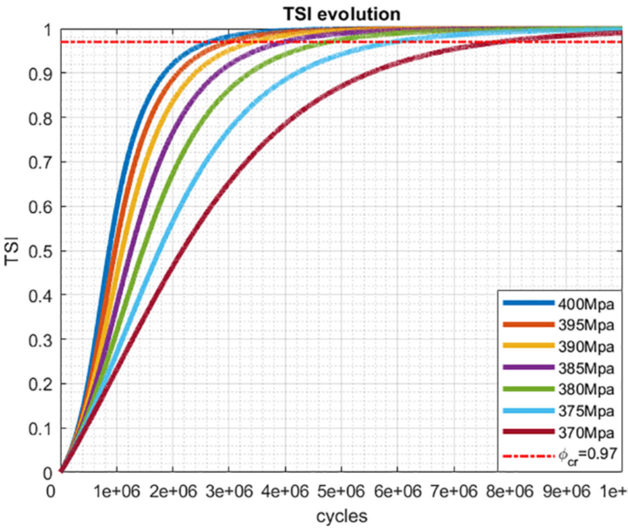

Fig. 4-4. TSI evolution versus cycles for 1.0577 steel under various stress amplitudes.

frequency [i.e., (Lee and Basaran, 2021; Ribeiro et al., 2020; Naderi et al., 2009). It is usually used as a damage indicator to predict the number of cycles to failure because if the theoretical cumulative specific entropy production of the material reaches the FFE, the specimen can be considered as reached the end of its thermodynamic life span. In Fig. 4-4, the TSI evolution that travels between 0 and 1. The evolution of TSI is based on the cumulative specific entropy production of the system, therefore for the same critical TSI ($\phi_{cr} = 0.999$), the cumulative specific entropy production of the specimen will be the same regardless of the stress amplitude, or frequency of loading or geometry of the sample, as shown in Fig. 4-3. This specific entropy value is the FFE. However, the time it takes to reach FFE will be different in each case (Fig. 4.5).

The comparison of unified mechanics theory-based model simulation S-N curve and the experimental S-N curve is presented in Fig. 4-6.

From Fig. 4-3, it is observed that the cumulative entropy generation for 1.0577 steel under various stress amplitude is the same ($4.1\mathrm{MJK^{-1}m^{-3}}$) at failure. This constant is the Fatigue Fracture Entropy that is a material property regardless of the test frequency, loading type, geometry of the specimen, or stress state. This has been also reported in the literature before (Naderi et al., 2009; Yun and Modarres, 2019), extensively.

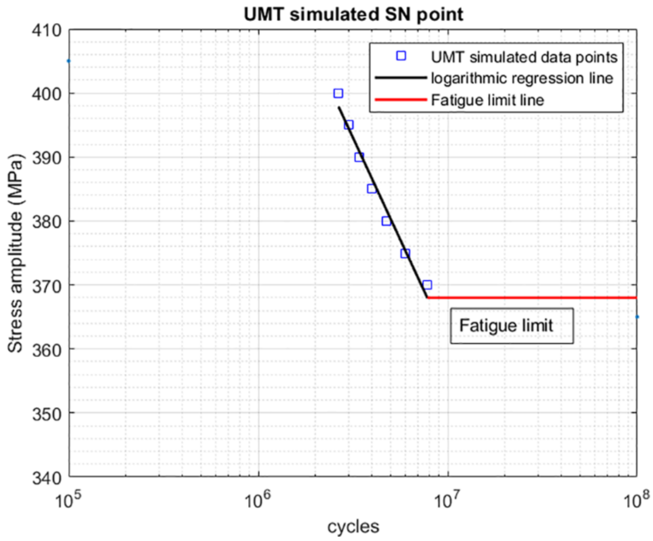

Fig. 4-5. Unified mechanics theory simulated S-N data points for 1.0577 steel under various stress amplitudes.

5. Conclusions

A unified mechanics theory-based model is used for predicting the very high cycle fatigue life of EN 1.0577 steel under ultrasonic vibration operating at 20 kHz. The thermodynamic fundamental equation of metals under ultrasonic fatigue is derived. Contributions of different mechanisms to the total entropy change are compared. The entropy generation due to microplasticity, thermal conduction, and atomic-friction generated heat are the dominant entropy generation mechanisms.

Microplasticity, which makes the biggest contribution to entropy generation, can be visualized as having a number of microplastic inclusions at defect sites in an elastic matrix which has its own micro-stress, and micro-strain based on laws of localization and homogenization. Energy is dissipated through the micro-plastic work at the locations of these inclusions. The number of inclusions increase as TSI ϕ increases from 0 to the predefined ϕ_{cr}. The evolution trend of numbers of inclusions leads to very little entropy generation in the beginning because in the beginning very few inclusion sites are activated. However, after cycles accumulate, the number of inclusions experiencing micro-plasticity gradually increases and entropy generation due to micro-plasticity becomes more evident.

While microplastic strain has been used as a variable for high cycle fatigue life modeling before, the evolution function has always been based on an empirical function which requires curve fitting parameters. In comparison, unified mechanics theory utilizes microplasticity dissipated energy for entropy generation calculations, only. The degradation evolution function in unified mechanics theory is based on the second law of thermodynamics in Boltzmann entropy equation form, which does not need empirical curve fitting parameters for fatigue damage evolution.

To obtain the absolute temperature of the specimen needed in the thermodynamic fundamental equation without test data, a fully coupled thermo mechanical equation that includes a heat storage term, a heat conduction term, a microplasticity term, and a self-heating term due to internal frictions, is derived. However, the derived thermal mechanical equation cannot capture the abrupt temperature rise in phase 3 when macro cracks initiate because the mechanisms of macro-plasticity, crack formation and crack propagation are not included in the model.

Very high cycle fatigue life prediction results based on the unified mechanics theory are compared with experimental test data. The comparison shows that the prediction and test data match very well.

Declaration of Competing Interest

The authors declare that they have no known competing financial interests or personal relationships that could have appeared to influence the work reported in this paper.

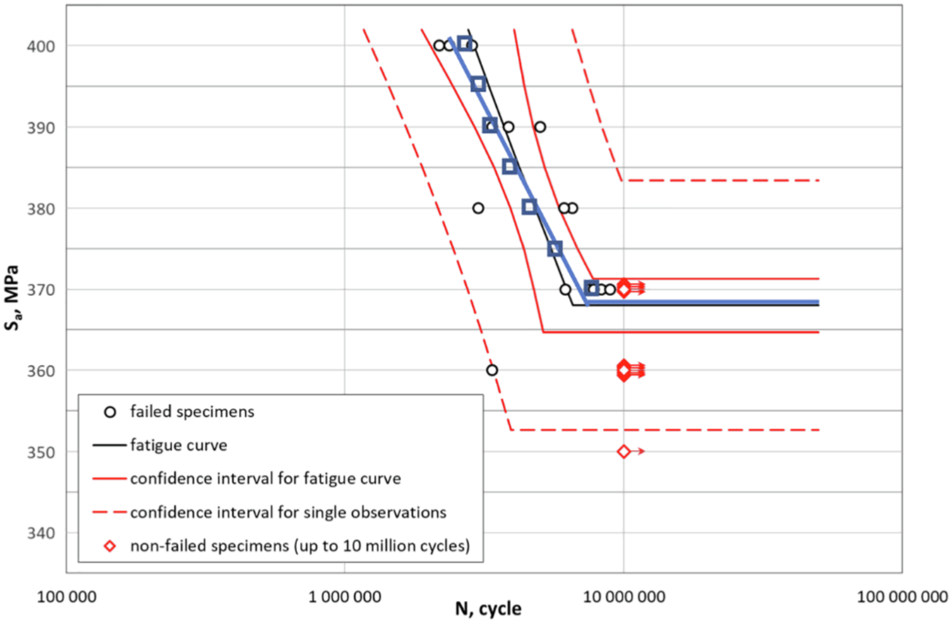

Fig. 4-6. UMT simulated S-N data points for 1.0577 steel compared with experimental data. The blue line and squares are simulated results from UMT. (For interpretation of the references to colour in this figure legend, the reader is referred to the web version of this article.)

References

Abbaschian, R., Abbaschian, L., & Reed-Hill, R., 2010, Physical metallurgy principles. Cengage Learning. ISBN 9780495438519.

Basaran, C., Chandaroy, R., 2000. Using finite element analysis for simulation of reliability tests on solder joints in microelectronic packaging. Comput. Struct. 74 (2), 215–231. https://doi.org/10.1016/s0045-7949(99)00028-0.

Basaran, C., Lin, M., Ye, H., 2003. A thermodynamic model for electrical current induced damage. Int. J. Solids Struct. 40 (26), 7315–7327. https://doi.org/10.1016/j.ijsolstr.2003.08.018.

Basaran, C., Lin, M., 2007. Damage mechanics of electromigration in microelectronics copper interconnects. Int. J. Mater. Struct. Integrity 1 (1/2/3), 16. https://doi.org/10.1504/ijmsi.2007.013864.

Basaran, C., Lin, M., 2007. Electromigration induced strain field simulations for nanoelectronics lead-free solder joints. Int. J. Solids Struct. 44 (14–15), 4909–4924. https://doi.org/10.1016/j.ijsolstr.2006.12.011.

Basaran, C., Li, S., Abdulhamid, M., 2008. Thermomigration induced degradation in solder alloys. J. Appl. Phys. 103 (12), 123520 https://doi.org/10.1063/1.2943261.

Basaran, C., Lin, M., 2008. Damage mechanics of electromigration induced failure. Mech. Mater. 40 (1–2), 66–79. https://doi.org/10.1016/j.mechmat.2007.06.006.

Basaran, C., Nie, S., 2004. An irreversible thermodynamics theory for damage mechanics of solids. Int. J. Damage Mech. 13 (3), 205–223. https://doi.org/10.1177/1056789504041058.

Basaran, C., Yan, C., 1998. A thermodynamic framework for damage mechanics of solder joints. J. Electron. Packag. 120 (4), 379–384. https://doi.org/10.1115/1.2792650.

Basaran, C., Li, S., Hopkins, D., Veychard, D., 2009. Electromigration time to failure of SnAgCuNi solder joints. J. Appl. Phys. 106 (1), 013707 https://doi.org/10.1063/1.3159012.

Basaran, C., Cartwright, A., Zhao, Y., 2001. Experimental damage mechanics of microelectronics solder joints under concurrent vibration and thermal loading. Int. J. Damage Mech. 10 (2), 153–170. https://doi.org/10.1106/hlb3-mjc8-jvyl-9a9p.

Basaran, C., Zhao, Y., Tang, H., Gomez, J., 2004. A damage-mechanics-based constitutive model for solder joints. J. Electron. Packag. 127 (3), 208–214. https://doi.org/10.1115/1.1939822.

Basaran, C., 2021. Introduction to Unified Mechanics Theory with Applications (1st ed.). Springer Nature: Berlin/Heidelberg, Germany, 2021; ISBN 978-3-030-57772-8.

Bathias, C., Paris, P., 2005. Gigacycle Fatigue in Mechanical Practice. Marcel Dekker, New York.

Bergström, Y., Granbom, Y., Sterkenburg, D., 2010. A dislocation-based theory for the deformation hardening behavior of DP steels: impact of martensite content and ferrite grain size. J. Metallurgy 2010, 1–16. https://doi.org/10.1155/2010/647198.

Bin Jamal, M.N., Kumar, A., Lakshmana Rao, C., Basaran, C., 2019. Low cycle fatigue life prediction using unified mechanics theory in Ti-6Al-4V Alloys. Entropy 22 (1), 24. https://doi.org/10.3390/e22010024.

Blaschke, D., 2019. Properties of dislocation drag from phonon wind at ambient conditions. Materials 12 (6), 948. https://doi.org/10.3390/ma12060948.

Blaschke, D., Mottola, E., Preston, D., 2019. Dislocation drag from phonon wind in an isotropic crystal at large velocities. Philos. Mag. 100 (5), 571–600. https://doi.org/10.1080/14786435.2019.1696484.

Blaschke, D.N., Mottola, E., Preston, D.L., 2020. Dislocation drag from phonon wind in an isotropic crystal at large velocities. Philos. Mag. 100, 571–600. https://doi.org/10.1080/14786435.2019.1696484.

Boltzmann, L., 1877. Uber die Beziehung zwischen dem zweiten Hauptsatze des mechanischen Wärmetheorie und der Wahrscheinlichkeitsrechnung, respective den Sätzen über das Wärmegleichgewicht. [On the relation between the second law of the mechanical theory of heat and the probability calculus with respect to theorems of thermal equilibrium]. Wiener Berichte II, vol. 76, pp. 373-435.

Bryant, M.D, Khonsari, M.M, and Ling, F.F., 2008, On the thermodynamics of degradation Proc. R. Soc. A.4642001–2014 doi:10.1098/rspa.2007.0371.

Callister, W., & Rethwisch, D., 2018. Materials science and engineering (10th ed.). ISBN: 9781119405498.

Charkaluk, E., Constantinescu, A., 2009. Dissipative aspects in high cycle fatigue. Mech. Mater. 41 (5), 483–494. https://doi.org/10.1016/j.mechmat.2009.01.018.

Chrysochoos, A., Boulanger, T., Morabito, A., 2012. Dissipation and thermoelastic coupling associated with fatigue of materials. Mech., Models Methods Civ. Eng. 147–156 https://doi.org/10.1007/978-3-642-24638-8_7.

Chu, Y., Gautreau, P., Ragab, T., Basaran, C., 2015. Temperature Dependence of Joule Heating in Zigzag Graphene Nanoribbon. Carbon 89, 169–175.

Cugy, P., Galtier, A., 2002. Microplasticity and temperature increase in low carbon steels. In: Blom, A.F. (Ed.), Proc. 8th Int. Fatigue Congress – 3–7 June 2002. EMAS, Barnsley, pp. 549–556.

Davoudi, K., Vlassak, J., 2018. Dislocation evolution during plastic deformation: equations vs. discrete dislocation dynamics study. J. Appl. Phys. 123 (8), 085302 https://doi.org/10.1063/1.5013213.

De Hosson, Th.M., Roos, A., Me, E.D.J., 2001. Temperature rise due to fast-moving dislocations. Philos. Mag. A 81 (5), 1099–1120. https://doi.org/10.1080/01418610110033975.

Dingley, D., Hale, K., 1966. Burgers vectors of dislocations in deformed iron and iron alloys. Proc. R. Society London Series A. Mathematical Phys. Sci. 295 (1440), 55–71. https://doi.org/10.1098/rspa.1966.0225.

Dixon, W., 1965. The up-and-down method for small samples. J. Am. Stat. Assoc. 60 (312), 967–978. https://doi.org/10.1080/01621459.1965.10480843.

Dixon, W., Mood, A., 1948. A method for obtaining and analyzing sensitivity data. J. Am. Stat. Assoc. 43 (241), 109–126. https://doi.org/10.1080/01621459.1948.10483254.

Doudard, C., Calloch, S., Cugy, P., Galtier, A., Hild, F., 2005. A probabilistic two-scale model for high-cycle fatigue life predictions. Fatigue Fract. Eng. Mater. Struct. 28 (3), 279–288. https://doi.org/10.1111/j.1460-2695.2005.00854.x.

Egner, W., Sulich, P., Mroziński, S., Egner, H., 2020. Modelling thermo-mechanical cyclic behavior of P91 steel. Int. J. Plast. 135, 102820 https://doi.org/10.1016/j.ijplas.2020.102820.

Fan, J., Zhao, Y., Guo, X., 2018. A unifying energy approach for high cycle fatigue behavior evaluation. Mech. Mater. 120, 15–25. https://doi.org/10.1016/j.mechmat.2018.02.001.

Freitas, Manuel, Reis, Luis, Anes, Vitor, Montalvão, Diogo, Ribeiro, A., Fonte, Manuel, 2011. Design and assembly of an ultrasonic fatigue testing machine. Anales de Mecánica de la Fractura. 1, 335–340.

Fultz, B., 2010. Vibrational thermodynamics of materials. Prog. Mater Sci. 55 (4), 247–352. https://doi.org/10.1016/j.pmatsci.2009.05.002.

Galligan, J., McKrell, T., Robson, M., 2000. Dislocation drag processes. Mater. Sci. Eng.: A 287 (2), 259–264. https://doi.org/10.1016/s0921-5093(00)00783-8.

Gao, S., 1997. Quantum kinetic theory of vibrational heating and bond breaking by hot electrons. Phys. Rev. B 55 (3), 1876–1886. https://doi.org/10.1103/physrevb.55.1876.

General and perturbation procedures. Abaqus-docs.mit.edu. (2021). Retrieved 14 May 2021, from https://abaqus-docs.mit.edu/2017/English/SIMACAEANLRefMap/simaanl-c-linearnonlinear.htm#simaanl-c-linearnonlinear-linperturbation.

Guo, Q., Guo, X., Fan, J., Syed, R., Wu, C., 2015. An energy method for rapid evaluation of high-cycle fatigue parameters based on intrinsic dissipation. Int. J. Fatigue 80, 136–144. https://doi.org/10.1016/j.ijfatigue.2015.04.016.

Hajshirmohammadi, B., Khonsari, M., 2020. On the entropy of fatigue crack propagation. Int. J. Fatigue 133, 105413. https://doi.org/10.1016/j.ijfatigue.2019.105413.

He, S., He, B., Zhu, K., Huang, M., 2018. Evolution of dislocation density in bainitic steel: modeling and experiments. Acta Mater. 149, 46–56. https://doi.org/10.1016/j.actamat.2018.02.023.

Ho, H., Risbet, M., Feaugas, X., 2017. A cyclic slip irreversibility based model for fatigue crack initiation of nickel base alloys. Int. J. Fatigue 102, 1–8. https://doi.org/10.1016/j.ijfatigue.2017.04.007.

Huang, M., Rivera-Díaz-del-Castillo, P., Bouaziz, O., van der Zwaag, S., 2008. Irreversible thermodynamics modelling of plastic deformation of metals. Mater. Sci. Technol. 24 (4), 495–500. https://doi.org/10.1179/174328408x294125.

Jamal, M.N., Rao, C., Basaran, C., 2021. A unified mechanics theory-based model for temperature and strain rate dependent proportionality limit stress of mild steel. Mech. Mater. 155, 103762 https://doi.org/10.1016/j.mechmat.2021.103762.

Kelly, A., Knowles, K., 2012. Crystallography and Crystal Defects. Wiley, MA.

Kondepudi, D., & Prigogine, I., 2014. Modern Thermodynamics: From heat engines to dissipative structures. doi:10.1002/9781118698723.

Kröner, E., 1961. Zur plastischen verformung des vielkristalls. Acta Metall. 9 (2), 155–161. https://doi.org/10.1016/0001-6160(61)90060-8.

Lee, H.W., Basaran, C., 2021, Predicting High Cycle Fatigue Life with Unified Mechanics Theory. Mech. Mater. (Submitted April 2021).

Lee, H.W., Basaran, C., 2021. A review of damage, void evolution, and fatigue life prediction models. Metals 11 (4), 609.

Lemaitre, J., Chaboche, J., 1990. Mech. Solid Mater. https://doi.org/10.1017/cbo9781139167970.

Lemaitre, J., Sermage, J., Desmorat, R., 1999. A two scale damage concept applied to fatigue. Int. J. Fract. 97 (1/4), 67–81. https://doi.org/10.1023/a:1018641414428.

Li, S., Abdulhamid, M., Basaran, C., 2008. Simulating damage mechanics of electromigration and thermomigration. Simulation 84 (8–9), 391–401. https://doi.org/10.1177/0037549708094856.

Li, S., Abdulhamid, M., Basaran, C., 2009. Damage mechanics of low temperature electromigration and thermomigration. IEEE Trans. Adv. Packag. 32 (2), 478–485. https://doi.org/10.1109/tadvp.2008.2005840.

Marti, N., Favier, V., Gregori, F., Saintier, N., 2020. Correlation of the low and high frequency fatigue responses of pure polycrystalline copper with mechanisms of slip band formation. Mater. Sci. Eng.: A 772, 138619. https://doi.org/10.1016/j.msea.2019.138619.

Mehdizadeh, M., Haghshenas, A., Khonsari, M., 2021. On the effect of internal friction on torsional and axial cyclic loading. Int. J. Fatigue 145, 106113. https://doi.org/10.1016/j.ijfatigue.2020.106113.

Messerschmidt, U., Bartsch, M., 2003. Generation of dislocations during plastic deformation. Mater. Chem. Phys. 81 (2–3), 518–523. https://doi.org/10.1016/s0254-0584(03)00064-6.

Mughrabi, H., 2002. On 'multi-stage' fatigue life diagrams and the relevant life-controlling mechanisms in ultrahigh-cycle fatigue. Fatigue Fract. Eng. Mater. Struct. 25 (8–9), 755–764. https://doi.org/10.1046/j.1460-2695.2002.00550.x.

Mughrabi, H., 2009. Cyclic slip irreversibilities and the evolution of fatigue damage. Metal. Mater. Trans. A 40 (6), 1257–1279. https://doi.org/10.1007/s11661-009-9839-8.

Mughrabi, H., 2013. Cyclic slip irreversibility and fatigue life: a microstructure-based analysis. Acta Mater. 61 (4), 1197–1203. https://doi.org/10.1016/j.actamat.2012.10.029.

Naderi, M., Amiri, M., Khonsari, M., 2009. On the thermodynamic entropy of fatigue fracture. Proc. R. Soc. A: Mathematical, Phys. Eng. Sci. 466 (2114), 423–438. https://doi.org/10.1098/rspa.2009.0348.

Nobutada Ohno, section 4.6 - Kinematic Hardening Rule with Critical State of Dynamic Recovery, Editor(s): JEAN LEMAITRE, Handbook of Materials Behavior Models, Academic Press, 2001, Pages 232-239, ISBN 9780124433410, doi:10.1016/B978-012443341-0/50025-9.

Osara, Bryant, 2019. Thermodynamics of fatigue: degradation-entropy generation methodology for system and process characterization and failure analysis. Entropy 21 (7), 685. https://doi.org/10.3390/e21070685.

Parvin, H., Kazeminezhad, M., 2016. Modelling the temperature rise effect through high-pressure torsion. Mater. Sci. Technol. (United Kingdom) 32, 1218–1222. https://doi.org/10.1080/02670836.2015.1114713.

Planck, M., 1900, Section 134: Entropie und Warscheinlichkeit. In Vorlesungen uber die theorie der wurmestrahlung; J.A. Barth: Leipzig, Germany.

Ragab, T., Basaran, C., 2009. Joule heating in single-walled carbon nanotubes. J. Appl. Phys. 106, 063705.

Ribeiro, P., Petit, J., Gallimard, L., 2020. Experimental determination of entropy and exergy in low cycle fatigue. Int. J. Fatigue 136, 105333. https://doi.org/10.1016/j.ijfatigue.2019.105333.

Shanthraj, P., Zikry, M., 2011. Dislocation density evolution and interactions in crystalline materials. Acta Mater. 59 (20), 7695–7702. https://doi.org/10.1016/j.actamat.2011.08.041.

Temfack, T., Basaran, C., 2015. Experimental verification of thermodynamic fatigue life prediction model using entropy as damage metric. Mater. Sci. Technol. 31 (13), 1627–1632. https://doi.org/10.1179/1743284715y.0000000074.

Teng, Z., Wu, H., Boller, C., Starke, P., 2020. Thermodynamic entropy as a marker of high-cycle fatigue damage accumulation: example for normalized SAE 1045 steel. Fatigue Fract. Eng. Mater. Struct. 43 (12), 2854–2866. https://doi.org/10.1111/ffe.13303.

Torabian, N., Favier, V., Dirrenberger, J., Adamski, F., Ziaei-Rad, S., Ranc, N., 2017. Correlation of the high and very high cycle fatigue response of ferrite based steels with strain rate-temperature conditions. Acta Mater. 134, 40–52. https://doi.org/10.1016/j.actamat.2017.05.064.

Viatkina, E., Brekelmans, W., Geers, M., 2007. Modelling the evolution of dislocation structures upon stress reversal. Int. J. Solids Struct. 44 (18–19), 6030–6054. https://doi.org/10.1016/j.ijsolstr.2007.02.010.

Voyiadjis, George, Abed, Farid, 2005. Effect of dislocation density evolution on the thermomechanical response of metals with different crystal structures at low and high strain rates and temperatures. Arch. Mech. 57.

Wang, J., Yao, Y., 2017. An entropy based low-cycle fatigue life prediction model for solder materials. Entropy 19 (10), 503. https://doi.org/10.3390/e19100503.

Wang, J., Yao, Y., 2019. An entropy-based failure prediction model for the creep and fatigue of metallic materials. Entropy 21 (11), 1104. https://doi.org/10.3390/e21111104.

Xue, H., Bayraktar, E., Bathias, C., 2007. Damage initiation mechanism of a nodular cast iron under the very high cycle fatigue regime. Int. J. Comput. Mater. Sci. Surf. Eng. 1 (6), 635. https://doi.org/10.1504/ijcmsse.2007.017920.

Yao, W., Basaran, C., 2012. Electromigration analysis of solder joints under ac load: a mean time to failure model. J. Appl. Phys. 111 (6), 063703 https://doi.org/10.1063/1.3693532.

Yao, W., Basaran, C., 2013. Electromigration damage mechanics of lead-free solder joints under pulsed DC: a computational model. Comput. Mater. Sci. 71, 76–88. https://doi.org/10.1016/j.commatsci.2013.01.016.

Yao, W., Basaran, C., 2013. Damage mechanics of electromigration and thermomigration in lead-free solder alloys under alternating current: an experimental study. Int. J. Damage Mech. 23 (2), 203–221. https://doi.org/10.1177/1056789513488396.

Yao, W., Basaran, C., 2013. Computational damage mechanics of electromigration and thermomigration. J. Appl. Phys. 114 (10), 103708 https://doi.org/10.1063/1.4821015.

Ye, H., Basaran, C., Hopkins, D., 2004. Deformation of solder joint under current stressing and numerical simulation—I. Int. J. Solids Struct. 41 (18–19), 4939–4958. https://doi.org/10.1016/j.ijsolstr.2004.04.002.

Ye, H., Basaran, C., Hopkins, D., 2006. Experimental damage mechanics of micro/power electronics solder joints under electric current stresses. Int. J. Damage Mech. 15 (1), 41–67. https://doi.org/10.1177/1056789506054311.

Young, Subbarayan, 2019. Maximum entropy models for fatigue damage in metals with application to low-cycle fatigue of aluminum 2024–T351. Entropy 21 (10), 967. https://doi.org/10.3390/e21100967.

Yun, H., Modarres, M., 2019. Measures of entropy to characterize fatigue damage in metallic materials. Entropy 21 (8), 804. https://doi.org/10.3390/e21080804.

Zhang, L., Liu, X., Wu, S., Ma, Z., Fang, H., 2013. Rapid determination of fatigue life based on temperature evolution. Int. J. Fatigue 54, 1–6. https://doi.org/10.1016/j.ijfatigue.2013.04.002.

Zhao, Y., Basaran, C., Cartwright, A., Dishongh, T., 2000. Thermomechanical behavior of micron scale solder joints under dynamic loads. Mech. Mater. 32 (3), 161–173. https://doi.org/10.1016/s0167-6636(99)00053-8.